

Influence of ZCuOH, Z₂Cu, and Extraframework Cu_xO_y Species in Cu-SSZ-13 on N₂O Formation during the Selective Catalytic Reduction of NO_x with NH₃

Arthur J. Shih,* Juan M. González, Ishant Khurana, Lucía Pérez Ramírez, Andres Peña L., Ashok Kumar, and Aída Luz Villa*



Cite This: *ACS Catal.* 2021, 11, 10362–10376



Read Online

ACCESS |



Metrics & More



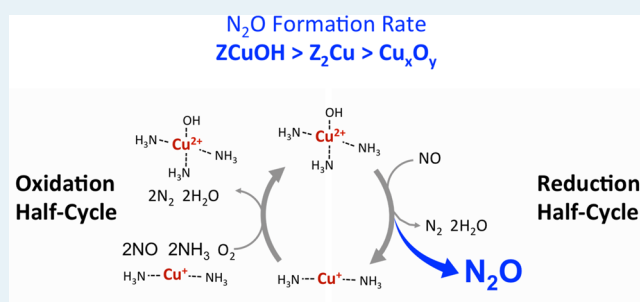
Article Recommendations



Supporting Information

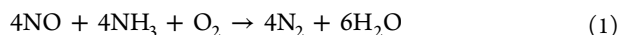
ABSTRACT: In this contribution, we synthesized three model Cu-SSZ-13 catalysts with primarily ZCuOH, Z₂Cu, and extraframework Cu_xO_y species and then measured their N₂O formation rates during standard selective catalytic reduction (SCR). We first present evidence that the formation of extraframework Cu_xO_y species after sequential aqueous ion exchange and calcination correlates with the formation of Cu(OH)₂ precipitates during ion exchange. These Cu_xO_y species are not active for standard SCR, and unchanged apparent activation energies and reaction orders demonstrate that these Cu_xO_y species do not induce transport limitations to accessible Cu²⁺ active centers. During standard SCR, N₂O formation rates on a per Cu basis were the fastest (and exhibited higher selectivities) on ZCuOH, followed by Z₂Cu and then extraframework Cu_xO_y. Because N₂O formation apparent activation energies were indistinguishable from the standard SCR apparent activation energies associated with the reduction-limited step, we posit that N₂O is formed during the standard SCR reduction step. Additionally, using sulfur poisons to force the ZCuOH rate-limiting step to the oxidation half-cycle resulted in an unchanged N₂O formation apparent activation energy, further supporting our hypothesis. These results suggest that utilizing Cu-SSZ-13 catalysts with higher fractions of Z₂Cu active centers in commercial aftertreatment systems can lead to reduced N₂O emissions.

KEYWORDS: NO_x SCR, N₂O, SO₂, Cu-SSZ-13, aqueous ion exchange, speciation, Cu oxides, redox



1. INTRODUCTION

Since the discovery of Cu zeolites as effective catalysts for the selective catalytic reduction (SCR) of NO_x from diesel engine exhaust by Iwamoto et al.¹ and Held et al.² in the early 1990s, the more hydrothermally stable Cu chabazite (CHA) SSZ-13 zeolites have been discovered, researched, and successfully implemented commercially.^{3–5} In heavy-duty diesel engine systems, N₂O is produced primarily from the combustion of fossil fuels and from aftertreatment processes,⁶ in particular during the NH₃ selective catalytic reduction (eq 1). N₂O emissions are regulated due to its estimated global warming potential of ~300 times that of CO₂ and its role in the depletion of stratospheric ozone.^{7–9} The concentration of N₂O in the atmosphere has historically hovered around 270 ppb; however, in the last 200 years it has increased by ~20% to 331 ppb.¹⁰ A fundamental understanding of how N₂O is produced over Cu-SSZ-13 would lead to improved Cu-SSZ-13 catalysts with lower N₂O emissions.



In an effort toward better understanding and control of the Cu-SSZ-13 catalyst, fundamental research into the SCR mecha-

nism, active sites, and deactivation from sulfur poisoning,^{11–14} phosphorous poisoning,¹⁵ and hydrothermal deactivation^{11,16} have undergone extensive research over the past decade. Cu²⁺ ions were first determined to be the active centers from both *in situ* spectroscopy and SCR kinetics where normalizing the differential SCR rate per Cu resulted in a constant turnover rate.^{17–19} It was later determined that Cu²⁺ active centers come in two states: Cu²⁺ ionically tethered to two neighboring anionic sites in the zeolite framework and (CuOH)⁺ ionically tethered to isolated anionic sites in the zeolite framework^{17,20–22} (hereby denoted as Z₂Cu and ZCuOH, respectively, where Z represents an anionic site on the zeolite framework). The relative fraction of these two copper species depends on the copper density in addition to the density and distribution of anionic sites in the zeolite framework.^{22,23} The

Received: April 24, 2021

Revised: July 20, 2021

more thermodynamically favorable Z_2Cu are exchanged first at paired anionic sites on the zeolite framework, followed by $ZCuOH$ at isolated anionic sites.²² *Operando* X-ray absorption spectroscopy (XAS) indicated that during SCR, Cu ion active centers catalyze the SCR reaction via a reduction–oxidation mechanism,²⁴ and both Z_2Cu and $ZCuOH$ were found to be solvated by NH_3 .^{22,25}

Further SCR research thrusts focused on elucidating atomic details of the reduction and oxidation half-cycles. During the reduction half-cycle, it is proposed that mononuclear $Cu(NH_3)_4^{2+}$ or $Cu(NH_3)OH^+$ reacts with NO to form nitrosoamide (NH_2NO) or ammonium nitrite (NH_4NO_2) intermediates, respectively, which dissociate to $Cu(NH_3)_2^+$, N_2 , and H_2O .^{22,26–28} A recent study by Gramigni et al., however, observed second-order kinetics from transients, suggesting that binuclear reactions between two Cu could possibly occur during the reduction half-cycle.²⁹ The reoxidation of $Cu(NH_3)_2^+$ back to $Cu(NH_3)_4^{2+}$ is proposed to proceed via a binuclear reaction between two $Cu(NH_3)_2^+$ and O_2 ^{25,30,31} to form a $Cu(NH_3)_2^+(O_2)Cu(NH_3)_2^+$ dimeric intermediate. Recent studies by Chen et al. propose that $Cu(NH_3)_2^+(O_2)-Cu(NH_3)_2^+$ reacts with NH_3 and NO to form $Cu(H_2NNO)^{2+}$ and $Cu(HONO)^{2+}$ intermediates, respectively, that decompose over neighboring Brønsted acid sites to complete the catalytic SCR cycle.^{32,33}

Because the oxidation half-cycle seems to require two $Cu(NH_3)_2^+$ with overlapping diffusion spheres^{25,31} and $Cu(H_2NNO)^{2+}$ or $Cu(HONO)^{2+}$ with overlapping diffusion spheres with Brønsted acid sites (H^+),^{31,32} it is predicted that a dilute Cu^+ density or H^+ density would render a fraction of isolated Cu^+ and H^+ species as inactive. This was observed with *in situ* XAS where O_2 was able to reoxidize fewer $Cu(NH_3)_2^+$ with decreasing Cu density.²⁵ In addition to changing the Cu^{2+} density and H^+ density, decreasing the O_2 pressure can result in a rate-limited oxidation half-cycle.³⁴

The literature overwhelmingly proposes two primary pathways for the nonselective formation of N_2O during SCR: (1) The decomposition of ammonium nitrate species formed from NH_3 and NO_x at low temperatures (<573 K) and (2) the oxidation of NH_3 with O_2 to N_2O at high temperatures (>573 K).^{35–37} Diffuse reflectance infrared Fourier transform spectroscopy (DRIFTS) of Cu-SSZ-13 treated with NO_2 and NH_3 indicated that ammonium nitrate is formed,³⁸ and upon temperature-programmed desorption (TPD),³⁹ N_2O and NO_2 are released up to temperatures ~ 593 K. This suggests that N_2O production during SCR at low temperatures could possibly originate from the thermal decomposition of ammonium nitrate. Furthermore, Chen et al.⁴⁰ utilized isotope-labeled *in situ* Fourier transform infrared (FTIR) and demonstrated from a stepwise ($NO_2 + O_2$) adsorption and then a ($^{15}NO + NH_3 + O_2$) reaction that surface nitrate groups may be responsible for the formation of the ammonium nitrate precursor to N_2O . A large excess of ammonium nitrate formed during SCR has also been shown to decrease the SCR rate, presumably poisoning the catalyst via pore blocking.^{41–43} At temperatures >573 K, many studies observed nonstoichiometric consumption of NH_3 and NO. Under these conditions, more NH_3 than NO was consumed concurrent with increases in N_2O production, leading to the claim that NH_3 oxidation is the dominant source of N_2O above ~ 573 K.^{36,37,44} Zhang et al. postulated from reaction kinetics that N_2O was produced via an Eley–Rideal mechanism above ~ 573 K.⁴⁵

Many of these N_2O formation studies include NO_2 in the feed gas, which is essentially absent for standard SCR. Two recent studies by Xi et al.⁴⁶ and Feng et al.⁴⁷ seem to refute the presence of ammonium nitrate as a possible intermediate for N_2O formation during standard SCR. Xi et al.⁴⁶ demonstrated using *in situ* DRIFTS that nitrate species are not detected during low-temperature standard SCR and that N_2O formation correlates with the amount of reducible Cu-SSZ-13 with NO and NH_3 . Feng et al.⁴⁷ utilized density functional theory (DFT) calculations and demonstrated that the decomposition of ammonium nitrate is unfavorable relative to the decomposition of H_2NNO species over Cu-OOH-Cu.

The effect of SCR gas pressures (NO_2 , NO, H_2O , NH_3 , O_2) on the N_2O selectivity during low-temperature (<573 K) SCR has also been studied in the literature. First of all, the presence of NO_2 in the aftertreatment exhaust system is of commercial interest because sources of NO_2 upstream of the SCR unit originate from combustion in the engine and oxidation of NO to NO_2 by the diesel oxidation catalyst (DOC). The presence of NO_2 in the feed instigates the fast SCR pathway,^{48,49} which unlike the standard SCR pathway is proposed to be a single-site reaction that occurs on both Cu^{2+} and H^+ sites.^{25,41,50,51} In conjunction with all of these changes in the active centers, an increase in the NO_2 pressure is reported to increase N_2O selectivity.^{40,52–55} Although the presence of water between 0 and 12% does not significantly affect the standard SCR rate,^{25,37} Tarach et al.⁵⁶ (Cu-ZSM-5 and Cu-TNU-9) and Zhang et al.⁴⁵ (Cu-ZSM-5, Cu-SAPO-34, Cu-SSZ-13) reported that an increase in water increases the N_2O selectivity on Cu zeolites. At 523 K, Liu et al.⁵⁷ observed an increase in N_2O selectivity with increasing H_2O from 0 to 2% and a decrease in N_2O selectivity at water concentrations greater than 2%. The opposite trend was observed at 723 K where N_2O formation decreased with increasing H_2O concentration up to 2% and it increased with increasing concentrations greater than 2% H_2O . Liu et al.⁵⁷ reported that an increase in NH_3 pressure increases the N_2O selectivity on Cu-SSZ-13. Furthermore, both Liu et al.⁵⁷ and Zhang et al.⁴⁵ reported that an increase in O_2 pressure also increases the N_2O selectivity. Liu et al.⁵⁷ also reported that in the absence of NO (NH_3 oxidation reaction conditions), N_2O selectivities decrease to near zero at low temperature (<573 K).⁵⁷ Kubota et al.⁵⁸ also demonstrated a decrease in N_2O selectivity with an increase in NO pressure on H-AFX, which they attributed to NO reducing ammonium nitrate (NH_4NO_3) to ammonium nitrite (NH_4NO_2), which would then decompose to N_2 and H_2O .

The effect of the zeolite cage and channel sizes on N_2O selectivity is not clear and currently under debate. An overwhelmingly large fraction of studies on Cu zeolites (Cu-ZSM-5, Cu-SSZ-13, Cu-TNU-9, Cu-EMT) report that larger zeolite cages and channels correlate with higher N_2O selectivity during SCR.^{43,59–62} Chen et al.⁴⁰ reported that NH_4NO_3 is more stable on smaller-pore Cu-CHA than on Cu-BEA from temperature-programmed desorption (TPD) experiments. Delahay et al.⁵³ also observed that ion-exchanging Ba^{2+} into Cu-FAU decreased the N_2O selectivity, presumably by decreasing the cage volume. A recent study by Tarach et al.,⁵⁶ however, reported higher N_2O selectivities on smaller-pore Cu-ZSM-5 and Cu-TNU-9 than on larger-pore Cu-FER and Cu-Y. Utilizing DFT computations, Feng et al.⁴⁷ demonstrated that the predicted energy landscape for ammonium nitrate decomposition is indistinguishable regardless of being unconfined or confined in an Al-free CHA cage.

Overall, these observations led to postulates that confinement plays a fundamental role in determining the N_2O selectivity. However, we note that in many of these studies, SCR conversions varied widely, indicating that the NO , NH_3 , O_2 , and H_2O pressures varied widely axially through the packed-bed reactors. This is important because, as discussed in the previous paragraph, gas pressures also affect the N_2O selectivity and may skew results if not kept differential.

In addition to the gas pressures and size of zeolite cages and channels, the effect of the Cu and acid sites on N_2O selectivity have also been studied. Wang et al.⁶³ observed that an increase in the Cu density increases the N_2O selectivity during standard SCR. Similarly, on Cu-TNU-9, Tarach et al.⁵⁶ reported a correlation with the production of N_2O and the SCR rate and proposed that the production rate of N_2O is linked to the ease at which the active Cu center can cycle between 1+ and 2+ oxidation states. Xi et al.⁴⁶ observed that N_2O formation increases with an increasing number of reducible Cu quantified by flowing $\text{NO} + \text{NH}_3$, suggesting that N_2O likely occurs during the reduction of Cu^{2+} to Cu^{1+} . Furthermore, González et al.⁶⁴ observed that CuOH^+ active centers exhibit higher selectivities toward side reactions than Cu^{2+} active centers during SCR. Overall, the formation of N_2O has been ascribed to possibly occur over Cu sites in general,⁶³ CuOH^+ ,⁵⁷ Cu-OOH-Cu complexes,⁴⁷ and H^+ acid sites.⁴⁷

In this contribution, we first present the synthesis of model catalysts with controlled Cu speciation (Cu^{2+} , CuOH^+ , and extraframework Cu_xO_y) and then report the effects of Cu speciation on N_2O formation rates collected under differential standard SCR conversions. Results indicate that N_2O formation rates are the highest on CuOH^+ , followed by Cu^{2+} and then Cu_xO_y . Moreover, from N_2O formation kinetics (apparent activation energies and reaction orders), we associate the formation of N_2O with the SCR reduction half-cycle. This fundamental understanding will allow us to engineer, at the atomic level, commercial SCR catalysts that produce less undesirable N_2O .

2. EXPERIMENTAL AND METHODS

2.1. Synthesis of Zeolite Supports. SSZ-13 with Si/Al molar ratios of 4.5, 15, and 25 were synthesized. The first step consisted of obtaining a sodium form of the zeolite (Na-SSZ-13) by hydrothermal synthesis. Different procedures were used for high-aluminum (Si/Al = 4.5) and moderate-aluminum (Si/Al = 15 and 25) SSZ-13, as reported below and also outlined in previous publications.^{17,22,25}

High-aluminum Na-SSZ-13 (Si/Al = 4.5) zeolites were obtained by a procedure reported by Fickel et al.,⁶⁵ which is based on a patent by Zones.⁶⁶ Briefly, 37.5 g of sodium silicate (reagent grade, Sigma-Aldrich), 30.0 g of 0.1 M NaOH (standardized solution, Alfa Aesar), and 48.0 g of deionized water (18.2 M Ω -cm at 298 K, Milli-Q) were added into a perfluoroalkoxy alkane (PFA) jar (Saville Corporation) and stirred with a magnetic Teflon stir bar for 15 min under ambient conditions. We note that use of glass jars must be avoided due to the undesirable dissolution of glass at high pH. About 3.75 g of $\text{NH}_4\text{-Y}$ zeolite (Si/Al = 2.6, Zeolyst CBV 300) was added and then stirred for an additional 30 min under ambient conditions. The resulting mixture was transferred to several 45 mL Teflon-lined stainless-steel autoclaves (Parr Instruments). The autoclaves were then secured to a tumbling plate in a forced convection oven (Yamato DKN-402C) at 413 K and rotated at 60 rotation per minute (RPM) for 6–10 days,

after which they were removed and immediately quenched in ambient water.

Moderate-aluminum Na-SSZ-13 (Si/Al = 15 and 25) zeolites were obtained by a procedure adapted from Deka et al.,⁶⁷ which is based on a patent by Zones.⁶⁶ Briefly, 28.4 g of trimethyladamantylammonium hydroxide (25%, Sachem Inc.), 71.4 g of deionized water, and 0.87 g of aluminum hydroxide (99.9%, SPI Pharma) were added to a PFA jar (Saville Corporation) and stirred with a magnetic Teflon stir bar for 15 min under ambient conditions. For Si/Al 25 zeolites, 0.43 g of aluminum hydroxide was used instead. After stirring, 10 g of fumed silica (Cab-o-sil M-5) was added to the mixture and then stirred for 2 h under ambient conditions to allow solids in the mixture to dissolve. The gel was transferred to several 45 mL Teflon-lined stainless-steel autoclaves (Parr Instruments). All 45 mL Teflon autoclaves were filled to about 70% full to ensure that the autogenous pressure (pressure generated while heating) stays within recommended safety limits. The autoclaves were secured to a tumbling plate in a forced convection oven (Yamato DKN-402C) at 433 K and rotated at 60 RPM for 10 days, after which they were removed and immediately quenched in ambient water.

After hydrothermal synthesis, the zeolite crystals were separated via centrifugation and underwent alternating water and acetone (99.9 wt %, Sigma-Aldrich) washes (50 mL water or acetone per g zeolite) until the pH decreased to less than 8, after which the sample was washed with copious amounts of water and dried at 373 K in ambient air for 24 h or until dry. Once dry, the zeolite was finely crushed and calcined at 823 K under flowing dry air (AirZero, Indiana Oxygen) for 8 h. The resulting Na-SSZ-13 zeolite was converted to the NH_4 form by ion exchange with 100 $\text{g}_{\text{solution}} \text{g}_{\text{zeolite}}^{-1}$ of 0.1 M NH_4NO_3 (>99%, Sigma-Aldrich) 353 K for 10 h, washed three times with 50 mL water per gram and then dried at 373 K under ambient air for 24 h or until dry. The resulting $\text{NH}_4\text{-SSZ-13}$ was finely crushed and calcined at 823 K under flowing dry air (AirZero, Indiana Oxygen) for 8 h to obtain H-SSZ-13. The use of dry air for calcination is imperative to avoid the hydrolysis and dealumination of framework aluminum.^{16,68}

2.2. Ion Exchange of Cu onto Zeolites. Copper was ion-exchanged into H-SSZ-13 (Si/Al 4.5, 15, and 25) via aqueous ion exchange with $\text{Cu}(\text{NO}_3)_2$ (99.9%, Sigma-Aldrich). A pH meter (Mettler Toledo S20 SevenEasy pH meter with pH electrode InLab 413 SG) calibrated with pH standards (Hach buffer solutions: pH 4.01 (NIST) and pH 7.00 (NIST)) was used to track the pH during Cu-exchange. In some samples, 0.1 M NH_4OH (>99%, Sigma-Aldrich) was added dropwise to increase the pH. In other samples, no NH_4OH was added. Once the pH was stabilized (6–12 h, monitored using a pH meter), Cu-zeolite solids were separated via centrifugation and then washed three times with 50 mL of deionized water per gram zeolite. Samples were then dried at 373 K in ambient air in an oven for 24 h or until dry.

2.3. Precipitation Curves. Aqueous $\text{Cu}(\text{NO}_3)_2$ (99.9%, Sigma-Aldrich) solutions (0.0–0.2 M) were prepared with deionized water at ambient temperature (298 K). A quantity of 0.1 M NH_4OH was added dropwise to 10 mL of aqueous Cu salt solution while stirring until a solid precipitate was visibly observed, after which the final pH and mass of solution was measured. The final Cu molarity in solution (M_2) was calculated from a Cu mol balance (eq 2).

$$M_2 = \frac{\left(\frac{g_{\text{CuSalt}}}{\text{MW}_{\text{CuSalt}}} - \frac{\text{Cu wt \% } g_{\text{zeolite}}}{100 \text{ MW}_{\text{Cu}}} \right)}{V_2} \quad (2)$$

where g_{CuSalt} is the mass of the Cu salt used to obtain the initial Cu salt solution, $\text{MW}_{\text{CuSalt}}$ is the molecular mass of the Cu salt, Cu wt % is the weight % of Cu in the final dry Cu-zeolite measured from bulk elemental analysis techniques (AAS, Section 2.4), g_{zeolite} is the mass of zeolite after the Cu-exchange process, MW_{Cu} is the molecular weight of Cu (63.542 g mol⁻¹), and V_2 is the final volume in liters of the Cu-exchange slurry solution before separation.

2.4. Catalyst Characterization. Crystalline structures were confirmed by X-ray diffraction (XRD) using a Rigaku Smart Lab X-ray diffractometer with Cu K(α) radiation source ($\lambda = 0.154$ nm) operated at 1.76 kW. Approximately 15 mg of dry powder was loaded onto a low-volume zero-background Rigaku holder and flattened with a clean borosilicate microscope slide. The diffraction pattern was recorded from 4 to 80° 2θ with a step size of 0.01° 2θ and scan rate of 0.1 s⁻¹. All XRD patterns were normalized such that the maximum peak intensity was set to unity. All XRD spectra were collected <48 h after synthesis or calcination, unless otherwise specified.

UV–visible–NIR spectra were collected under ambient conditions using an Agilent Cary 5000 Varian equipped with a Harrick Scientific Praying Mantis diffuse reflectance optics system and cell. Barium sulfate (99%, Sigma-Aldrich) was used as a baseline standard. The barium sulfate standard and samples were all sieved (pelletized, ground, and sieved to a nominal size of 125–250 μm) prior to use. Approximately 0.1 g of powder was loaded into the sample cup and flattened with a clean borosilicate microscope slide. Reflectance versus wavenumber spectra were collected from 4000 to 53 000 cm⁻¹ at a scan rate of 2000 cm⁻¹ and were postprocessed to Kubelka–Munk units.⁶⁹

Si, Al, and Cu bulk compositions were quantified using atomic absorption spectroscopy (AAS) on a PerkinElmer AAnalyst 300. Care was taken to test and ensure that all bottles and droppers were free of metal impurities that may skew our measurements. About 20–50 mg of Cu-zeolite was weighed and transferred to a 60 mL high-density polyethylene (HDPE) bottle (60 mL Nalgene wide-mouth amber). Approximately, 2 mL of hydrofluoric acid (48%, Mallinckrodt Baker, Baker Analyzed A.C.S. Reagent) was added with a polyethylene dropper. The bottle was closed, then shaken vigorously for 2 s to ensure wetting of the Cu-zeolite with hydrofluoric acid and then left in a fume hood for at least 8 h. Extreme care must be taken when working with hydrofluoric acid as it is highly corrosive and will cause extreme burns. All HF work was performed within a fume hood with the sash as low as possible. A NIOSH tight-fitting gas mask equipped with a cartridge filter rated for hydrofluoric acid, splash mask, neoprene apron, neoprene gloves, and neoprene shoe covers were worn over the standard laboratory coat, long pants, closed-toed shoes, and nitrile gloves. Approximately 50 mL of deionized water (18.2 M Ω -cm at 298 K, Milli-Q) was used to dilute the solution to concentrations within the AAS calibration range for Cu, Si, and Al. The mass of Cu-SSZ-13, mass of HF, and mass of deionized water were weighed by difference and recorded throughout this process.

Silicon AAS standards were prepared by diluting a 1000 ppm silicon AAS standard solution (Sigma-Aldrich, TraceCERT, 1000 mg L⁻¹ Si in NaOH) to 15, 75, and 150 ppm. These

silicon concentrations span the linear range reported in the PerkinElmer AAS manual. A linear calibration of the measured absorbance at 251.6 nm was used to determine the weight percent of silicon. Analogous procedures were followed to determine the weight percent of copper (Sigma-Aldrich, TraceCERT, 1000 mg L⁻¹ Cu in nitric acid) at 324.8 nm and aluminum (Sigma-Aldrich, TraceCERT, 1000 mg L⁻¹ Al in nitric acid) at 309.3 nm.

2.5. Kinetic Measurements. Kinetic measurements were performed in a 0.5 cm inner diameter tubular quartz reactor with a coarse quartz frit located in the middle of the tube to hold the catalyst bed. Briefly, 5–50 mg of the catalyst (pelletized, ground, and sieved to a nominal size of 0.125–0.250 mm diameter) was diluted with either inert carbon beads (0.3 mm diameter, HTW GmbH) or inert sieved silica gel (0.125–0.250 mm diameter, Fisher Chemical, Catalog no. S817-1) to minimize channeling effects and placed between two layers of quartz wool (Acros Organics AC451040500). Two K-type thermocouples (Omega) were placed within 2 mm above and below the catalyst bed to measure the temperature and confirm the absence of axial temperature gradients. A 1 cm high pile of quartz chips (~ 2 mm diameter) was placed on a stainless-steel wire mesh upstream of the catalyst to ensure proper gas mixing and plug flow. The loaded quartz tube was wrapped with aluminum foil and aluminum blocks to ensure contact with the heating element in the clamshell furnace (Applied Test Systems, Inc. Series 3210) for isothermal operation. The reactor system was leak-checked by pressurizing the system downstream of the mass flow controllers with He (UHP, 99.999%, Indiana Oxygen) at 35 kPa for at least 30 min prior to any data collection.

The simulated SCR exhaust conditions were 300 ppm NO (from 3.5% NO in balance Ar, Praxair), 300 ppm NH₃ (from 3.0% NH₃ in balance Ar, Praxair), 10% O₂ (from 99.5% O₂, commercial grade, Indiana Oxygen), 2.5% H₂O (from deionized water), 7% CO₂ (from liquid CO₂, Indiana Oxygen), and balance N₂ (from liquid N₂, Linde), at 1 atm and 473 K at total flow rates between 800 and 1500 mL min⁻¹. The catalyst loadings (5–50 mg), flow rates (800–1500 mL min⁻¹), and density of the catalyst bed (0.5 g mL⁻¹) correspond to gas hourly space velocities (GHSVs) between 480 000 and 9 000 000 h⁻¹. Effluent gases (NO, NH₃, CO₂, H₂O, NO₂, and N₂O) were analyzed by an MKS Multigas 2030 gas-phase FTIR spectrometer. A flow diagram of our reactor system is included in Figure S1. All steady-state kinetic measurements were collected under differential conversions (less than 20%) with SCR products cofed, allowing the use of algebraic CSTR design equations to compute SCR reaction rates^{70–74} (eq 3). Examples of typical steady-state kinetic measurement runs are shown in Figures S2 and S3. Because standard SCR was studied, reaction rates where equimolar NO and NH₃ consumption deviated by more than 10% were not included. This typically occurred at high concentrations of NO (>1000 ppm NO) where NO₂ formation and presumably fast SCR becomes significant. It should be noted that N₂O was not cofed as about 30 ppm N₂O was present in the NO tank (3.5% NO in balance Ar, Praxair). Once diluted, this resulted in ~ 0.25 ppm N₂O in our simulated SCR exhaust. Only differential (less than 20%) increases in the N₂O concentration were used to calculate N₂O formation kinetic parameters.

$$-r = \frac{(C_{\text{in}} - C_{\text{out}}) \dot{V}_{\text{total}}}{1000 \text{ 000} \frac{\text{PV}_{\text{total}}}{RT}} \quad (3)$$

r is the rate of NO reduction or N₂O formation, C is the concentration of NO or N₂O in ppm entering and leaving the catalyst bed, \dot{V}_{total} is the total flow rate, P is 1 atm, T is ambient temperature (298 K), and R is the universal gas constant. Reaction rate data were fitted to a power-law rate expression (eq 4) where $E_{\text{a,app}}$ is the apparent activation energy and α , β , γ , and δ are the apparent reaction orders with respect to concentrations of NO, NH₃, O₂, and H₂O, respectively. The experimentally measured apparent activation energies and reaction orders were used to interpolate experimentally measured reaction rates to standard SCR conditions (300 ppm, 300 ppm NH₃, 10% O₂, 2.5% H₂O, 7% CO₂, and balance N₂, at 1 atm and 473 K) using the power-law rate (eq 4) for fair comparison of reaction rates.

$$-r = A_0 \exp\left(-\frac{E_{\text{a,app}}}{RT}\right) C_{\text{NO}}^{\alpha} C_{\text{NH}_3}^{\beta} C_{\text{O}_2}^{\gamma} C_{\text{H}_2\text{O}}^{\delta} \quad (4)$$

3. RESULTS AND DISCUSSION

3.1. Synthesizing Model Catalysts with Extraframework Cu_xO_y

3.1.1. Formation of Cu(OH)₂ Precipitates at High pH. The incorporation of metal cations into anionic framework sites in zeolites is generally performed via aqueous ion exchange^{75–79} and the final Cu loading is governed primarily by the concentration of the metal in the exchange solution, the aluminum density and distribution in the zeolite framework, and the copper complexes formed in the exchange solution. Aqueous solutions of Cu(CH₃COO)₂, CuCl₂, CuSO₄, and Cu(NO₃)₂ have been used to exchange Cu²⁺ into SSZ-13^{17,65,67,80,81} and some copper complexes present in the aqueous ion-exchange solution may be sterically inhibited from diffusing through the pores and subsequently exchanging with Brønsted acid sites (BA) in the zeolite crystallite.^{22,25,82}

We postulate that these pore-diffusion limited species may be related to the formation of extraframework Cu_xO_y clusters⁸¹ and the decrease in SCR rates at high Cu densities,^{17,83–85} as shown in Figure 1.

As 0.1 M NH₄OH is added dropwise to aqueous Cu(NO₃)₂, Cu(OH)₂ precipitates as solids at a particular pH (hereafter

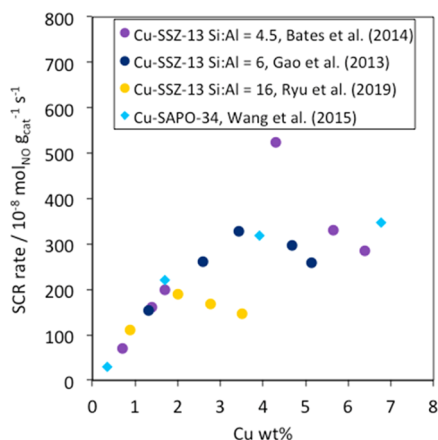


Figure 1. Standard SCR rate extracted from the literature and corrected to standard SCR conditions (300 ppm NH₃, 300 ppm NO, 10% O₂, 2.5% H₂O, 8% CO₂, and balance N₂ at 473 K and 1 atm total pressure) using eq 4. (For interpretation of the references to color in this figure legend, the reader is referred to the Web version of this article.)

called the precipitation pH). The pH at which Cu(OH)₂ precipitates from aqueous Cu²⁺ decreases with increasing molarity, consistent with the solubility model derived from thermodynamics (eqs 5 and 6). The complete derivation of the precipitation pH model as a function of pH can be found in the Supporting Information (Section S3). The precipitation pH curve for Cu(NO₃)₂ molarities between 0.005 and 0.2 M was measured (Figure 2), consistent with precipitation pH values

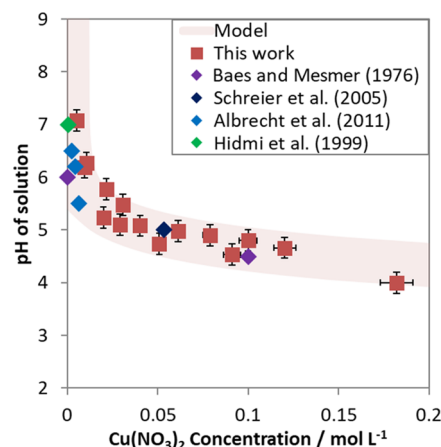
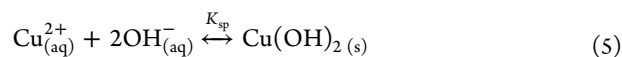


Figure 2. Equilibrium precipitation pH curve for Cu(NO₃)₂ using NH₄OH as a base to increase the pH. Cu(OH)₂ precipitates were observed above the curve. Literature values of Cu(NO₃)₂ precipitation from Baes and Mesmer⁸⁶ (purple diamonds), Schreier et al.⁸⁷ (dark blue diamonds), Albrecht et al.⁸⁸ (light blue diamonds), and Hidmi et al.⁸⁹ (green diamond) are included. A K_{sp} value of $5.5 \times 10^{20} \pm 4.5 \times 10^{20} \text{ L}^2 \text{ mol}^{-2}$ was obtained from fitting the experimental data to its thermodynamic solubility model (eq 6). (For interpretation of the references to color in this figure legend, the reader is referred to the Web version of this article.)

for Cu(NO₃)₂ reported by Baes and Mesmer,⁸⁶ Schreier et al.,⁸⁷ Albrecht et al.,⁸⁸ and Hidmi et al.⁸⁹ Precipitation pH curves for Cu(CH₃COO)₂ and CuSO₄ were also measured (Figures S5 and S6).



$$K_{\text{sp}} = \frac{1}{[\text{Cu}^{2+}] \left(\frac{K_{\text{w}}}{10^{-\text{pH}}}\right)^2} \quad (6)$$

K_{sp} values of $5.5 \times 10^{20} \pm 4.5 \times 10^{20} \text{ L}^2 \text{ mol}^{-2}$, $2.4 \times 10^{18} \pm 2.0 \times 10^{18} \text{ L}^2 \text{ mol}^{-2}$, and $4.1 \times 10^{21} \pm 3.9 \times 10^{21} \text{ L}^2 \text{ mol}^{-2}$ were obtained for Cu(NO₃)₂, Cu(CH₃COO)₂, and CuSO₄, respectively. We ascribe the large errors (calculated from repeats as 2 times the standard deviation to cover half of the data) to the fact that the data presented in this work represent independent repeats by three researchers in two different countries. When plotted against the literature (Figure 2), the scatter is in line with the reported data. For instance, Hidmi et al. reported a K_{sp} of $2.2 \times 10^{20} \text{ L}^2 \text{ mol}^{-2}$ for the precipitation of Cu(OH)₂ from an aqueous Cu(NO₃)₂, consistent with our measured Cu(NO₃)₂ solubility product.⁸⁹

3.1.2. Effect of Solution-Phase Cu(OH)₂ Precipitates on Cu Speciation in Cu Zeolites. Equilibrium pH and concentrations of all Cu-exchanged SSZ-13 samples synthesized are overlaid on the Cu-precipitation curve (Figure 3, zoom in in Figure S7). The pH of the solution (y -axis) designates the final pH of the

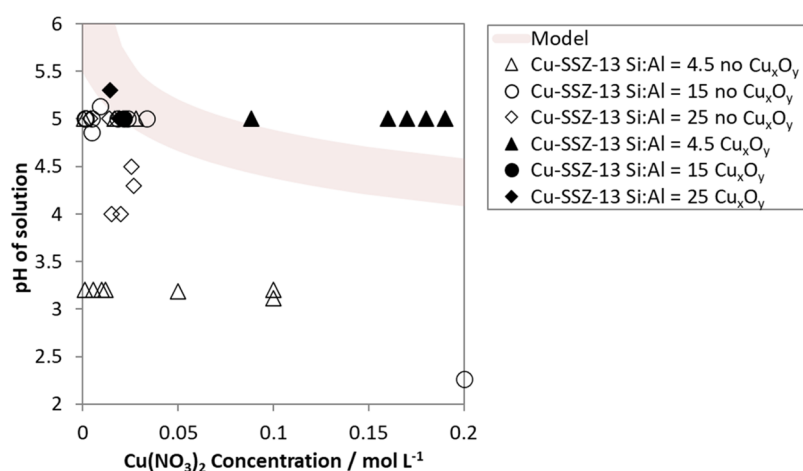


Figure 3. Equilibrium concentration of $\text{Cu}(\text{NO}_3)_2$ and pH after aqueous Cu-exchange of SSZ-13. Hollow shapes represent Cu-exchanged zeolites that did not exhibit black Cu_xO_y clusters after calcination. Filled black shapes represent Cu-exchanged zeolites that did exhibit black Cu_xO_y clusters after calcination. The precipitation pH for $\text{Cu}(\text{NO}_3)_2$ is represented by the best-fit precipitation curve model (light red trace). Zoom in into the cluster of data between 0 and 0.005 M $\text{Cu}(\text{NO}_3)_2$ can be found in Figure S4.

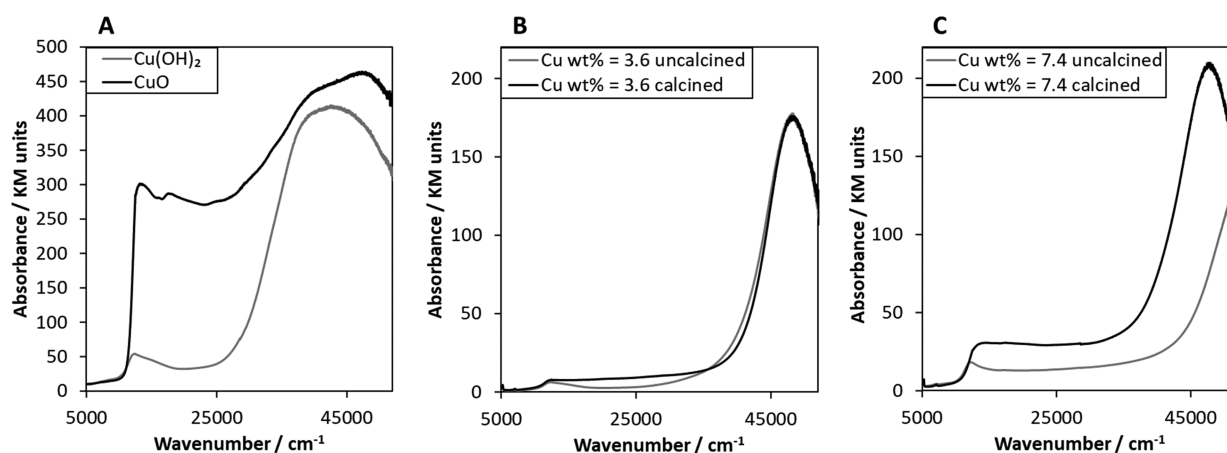


Figure 4. Diffuse reflectance UV–visible–NIR spectra collected under ambient conditions at 298 K of (A) $\text{Cu}(\text{OH})_2$ precipitate solids and CuO , (B) Cu-SSZ-13 Si/Al = 4.5 with Cu wt % of 3.6, and (C) Cu-SSZ-13 Si/Al = 4.5 with Cu wt % of 7.4. All Cu-SSZ-13 were Cu-exchanged in the $\text{Cu}(\text{OH})_2$ precipitation region.

slurry at equilibrium and the $\text{Cu}(\text{NO}_3)_2$ molarity is the molarity of the supernatant liquid after centrifuging out the solid Cu-SSZ-13 particles (x -axis) (eq 2). The presence of Cu_xO_y species can be detected using diffuse reflectance UV–visible–NIR or visually with the naked eye by the color of the sample (Figure S11) where samples with only Cu^{2+} ions are blue and samples with Cu_xO_y are gray/black. Samples that exhibit Cu_xO_y after calcination (filled shapes) appear either on or above the pH precipitation curve. Samples that exhibited no formation of Cu_xO_y clusters (hollow shapes) after calcination appear either on or below the pH precipitation curve. This suggests that precursors of Cu_xO_y species likely to come from $\text{Cu}(\text{OH})_2$ precipitates formed in solution during aqueous Cu-exchange. As such, we postulate that calcination in air (773 K in dry air, AirZero Indiana Oxygen) oxidizes $\text{Cu}(\text{OH})_2$ to Cu_xO_y , which agglomerates on and/or in the zeolite.

3.1.3. Identification of $\text{Cu}(\text{OH})_2$ Precipitates and Cu_xO_y Species Using UV–Visible and XRD. UV–visible (17 000–37 000 cm^{-1}) and XAS pre-edge (8.987 keV) features are indicative of Cu_xO_y species in Cu-SSZ-13.⁸¹ UV–visible–NIR spectra of only $\text{Cu}(\text{OH})_2$ precipitates and Cu_xO_y (Figure 4A) exhibit an increase in absorbance between 12 500 and 47 000

cm^{-1} in the Cu_xO_y spectra compared to $\text{Cu}(\text{OH})_2$. Figure 4B,C plots the UV–visible–NIR spectra on two Cu-SSZ-13 Si/Al = 4.5 samples Cu-exchanged above the pH precipitation curve before and after calcination. Before calcination, both samples showed distinct Cu^{2+} d–d transition and Cu–O ligand-to-metal charge transfer (LMCT) features at 12 500 and 47 000 cm^{-1} , respectively.^{17,67,90} After calcination, absorbance between 12 500 and 47 000 cm^{-1} increased, indicating that $\text{Cu}(\text{OH})_2$ species converted to CuO species during calcination.

XRD before and after calcination of Cu-SSZ-13 synthesized in the $\text{Cu}(\text{OH})_2$ precipitation region was used to identify and confirm the presence of Cu_xO_y species and $\text{Cu}(\text{OH})_2$ crystallites.^{91–93} $\text{Cu}(\text{OH})_2$ precipitates exhibit two sharp XRD features at 12.83 and 25.84° 2θ (Figure 5A). Cu_xO_y oxide clusters exhibit two sharp XRD features at 35.54 and 38.73° 2θ (Figure 5B). These features were used to determine the presence of $\text{Cu}(\text{OH})_2$ and Cu_xO_y crystalline particles on our Cu-SSZ-13 materials. The broad nature and weak intensity of $\text{Cu}(\text{OH})_2$ and Cu_xO_y in Cu-SSZ-13 XRD diffraction peaks are likely due to small particle sizes as Cu-SSZ-13 did not turn amorphous after synthesis and treatments, as evidenced by the

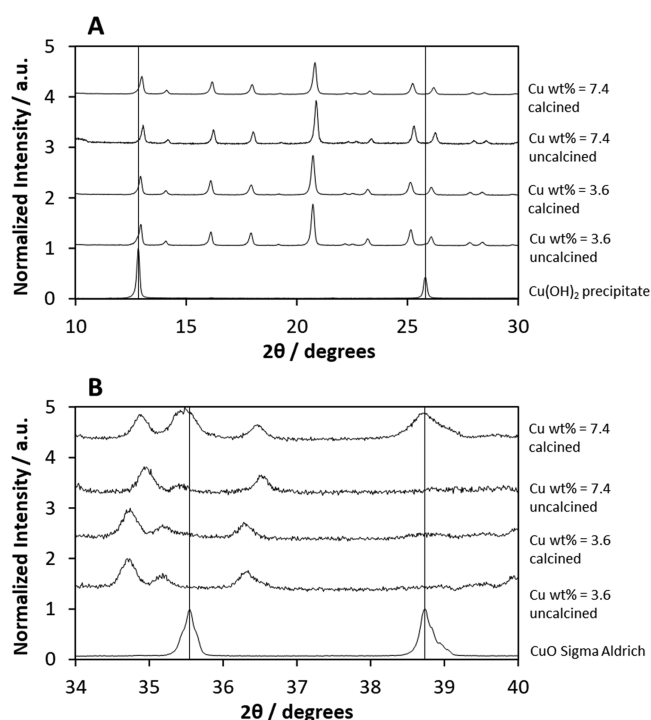


Figure 5. (A) XRD patterns from a 10 to 30° 2θ $\text{Cu}(\text{OH})_2$ precipitate and both uncalcined and calcined Cu-SSZ-13 Si/Al = 4.5 with Cu wt %'s of 3.6 and 7.4. (B) XRD patterns from 34 to 40° 2θ on CuO from Sigma-Aldrich and both uncalcined and calcined Cu-SSZ-13 Si/Al = 4.5 with Cu wt %'s of 3.6 and 7.4. Both Cu-SSZ-13 were Cu-exchanged in the $\text{Cu}(\text{OH})_2$ precipitation region.

unchanged broadness of the SSZ-13 diffraction peaks after aqueous Cu-exchange and calcination (Figure S13). Cu_xO_y was not detected on uncalcined Cu-SSZ-13 with Cu wt %'s of 3.6 and 7.4, and characteristic peaks of Cu_xO_y were observed in all Cu-SSZ-13 materials after calcination (Figure 5B). Uncalcined Cu-SSZ-13 materials did not show representative peaks of $\text{Cu}(\text{OH})_2$ materials, possibly due to the scarcity and/or small size of the $\text{Cu}(\text{OH})_2$ crystallites (Figure 5A).^{94,95} XRD and UV-visible-NIR characterization on a Cu-SSZ-13 sample (Si/Al = 4.5, Cu wt % = 18.9) is also presented in Figures S12–S15.

In summary, the presence of copper clusters in Cu-SSZ-13 after aqueous copper ion exchange and calcination was identified using XRD and UV-visible-NIR and found to be correlated with the pH of the copper-containing exchange solution. The overall Cu-exchange process is likely to be more nuanced as additional treatments may alter the location and fraction of extraframework Cu oxide species.⁹⁶ Additionally, we found that if the pH and Cu molarity during aqueous Cu ion exchange are too low, the deactivation of Brønsted acid sites (as probed using NH_3 titration) also occurs (Figure S16). We also copper-exchanged H-ZSM-5 (Si/Al = 12.5 and 30) and H- β (Si/Al = 11.5) with $\text{Cu}(\text{NO}_3)_2$ (99.9%, Sigma-Aldrich), $\text{Cu}(\text{CH}_3\text{COO})_2$ (98%, Sigma-Aldrich), or $\text{Cu}(\text{SO}_4)_2$ ($\geq 99\%$, Sigma-Aldrich) and found no significant dependencies between the anion and zeolite frameworks (Figures S8–S10).

3.2. Influence of ZH, Z_2Cu , ZCuOH , and Cu_xO_y Species on SCR Reaction Kinetics. 3.2.1. *Standard SCR Kinetics on Z_2Cu , ZCuOH , and Extraframework Cu_xO_y .* Figure 6 plots the SCR reaction rate as a function of Cu wt % for a series of Cu-SSZ-13 catalysts with Si/Al of 4.5, 15, 25, and 100, all Cu-

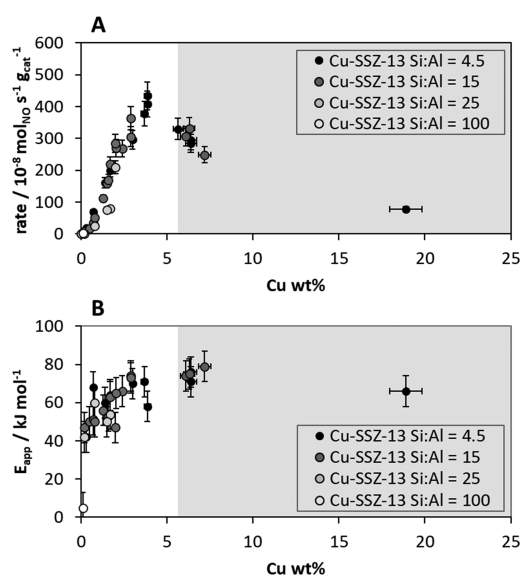


Figure 6. (A) Standard SCR rate normalized per gram of catalyst plotted versus Cu wt % and (B) standard SCR apparent activation energy plotted versus Cu wt %. Standard SCR conditions: 300 ppm NH_3 , 300 ppm NO, 10% O_2 , 2.5% H_2O , 8% CO_2 , and balance N_2 at 473 K and 1 atm total pressure. Cu-SSZ-13 catalysts with Si/Al molar ratios of 4.5 and 15 and Cu wt %s between 0 and 19 were synthesized and used for this study. The unshaded area between 0 and 4 wt % represents samples with all Cu as ionic $\text{Cu}^{2+}/\text{Cu}^{+}$ species. The gray shaded area between 4 and 19 wt % represents samples that contain extraframework Cu_xO_y species. NO, NH_3 , and O_2 reaction orders are plotted in Figures S18–S20.

exchanged at a pH of 5. We first note that ZH sites are not active for standard SCR as demonstrated by their insignificant SCR rate at a Cu wt % of 0. When copper exists as only ionic Z_2Cu and ZCuOH (0–4 Cu wt %), the reaction rates are indistinguishable from each other and increase nearly linearly with Cu wt %. This is interpreted as similar SCR reaction landscapes for both Z_2Cu and ZCuOH active centers, which was also demonstrated with DFT by Paolucci et al.²² The nonlinear parabolic-shaped increase in the SCR rate at low Cu densities and ZH densities correlates with lower apparent activation energies ($< \sim 50$ kJ mol^{-1}). Coupling these kinetic measurements with *operando* XAS demonstrated that the decrease in the apparent activation energy from ~ 70 to $< \sim 50$ kJ mol^{-1} can be attributed to a change in the rate-limiting step from reduction to oxidation limited, respectively.^{25,34} In this interpretation, dilute Cu densities disable the ability of $\text{Cu}(\text{NH}_3)_2^+$ to pair and form the proposed dimeric intermediate in the oxidation half-cycle.^{25,30}

A recent study by Feng et al. proposed that ZH sites are necessary in the oxidation half-cycle for fully oxidizing and splitting the Cu dimeric intermediate back to separate $\text{Cu}(\text{NH}_3)_4^{2+}$ intermediates. If true, we would predict a decrease in the SCR rate with a decrease in ZH sites. To test this prediction, we synthesized a Cu-SSZ-13 Si/Al = 100 sample where the ZH density was ~ 18 times lower than the ZH density on Si/Al = 4.5. Although we were unable to statistically differentiate the Cu-SSZ-13 Si/Al = 100 reaction rate from the other Cu-SSZ-13 with similar Cu densities due to low differential conversions near the detection limit of the MKS FTIR unit, we did measure a drastic decrease in the apparent activation energy to ~ 10 kJ mol^{-1} upon decreasing the ZH density (Figures 6 and S17). Within context of the

experimental kinetics collected at similar low Cu loadings between 0.1 and 0.2 wt %, increasing the Si/Al ratio from 4.5 to 25 to 100 corresponds to a systematic decrease in the apparent activation energy of ~ 70 to ~ 50 to ~ 10 kJ mol⁻¹ (Figures 6 and S17). This experimental observation from a decrease in ZH density is also consistent with another interpretation from impedance spectroscopy where Cu ions are able to diffuse and hop between anionic sites in the zeolite lattice.^{97,98} Although solely kinetics is unable to distinguish between these two mechanistic proposals, our kinetic results indicate that the ZH density does indeed play a role in influencing the oxidation half-cycle of the SCR mechanism.

When the presence of extraframework Cu_xO_y increases above a Cu wt % of 4 (corresponding to Cu-exchange at conditions above the Cu(OH)₂ precipitation line when exchanged at a pH of 5), the SCR reaction rate decreases while the apparent activation energy remains constant (Figure 6). This suggests that Cu_xO_y is inactive for SCR and decreases the SCR reaction rate by either (1) converting active sites (ionic Cu) into extraframework Cu_xO_y species or (2) pore blocking (mass transport effects). We postulate that the unchanged activation energy between 4 and 19 Cu wt % indicates that the remaining Cu²⁺ ions turn over or react via the same mechanistic SCR pathway, free of mass transport effects. One implication of this kinetic result is that if extraframework Cu_xO_y can disable Cu²⁺ centers from turning over by physically preventing reactants from reaching and/or products from leaving, they must do it by blocking all 6 possible 8-member ring entrances/exits of the chabazite cage. If only a fraction of the 8-member rings are blocked, then we presume a fraction of the active centers would be transport limited and the measured apparent activation energy would be ~ 35 kJ mol⁻¹, half of the transport-free ~ 70 kJ mol⁻¹.^{72,73} Since we do not observe any decrease in the apparent activation energy, it indicates that either none or an insignificant minority of the active Cu²⁺ centers is transport limited in the presence of extraframework Cu_xO_y – even when an overwhelmingly large fraction of the Cu exists as extraframework Cu_xO_y.

3.2.2. N₂O Formation Kinetics on Z₂Cu, ZCuOH, and Extraframework Cu_xO_y. Three Cu-SSZ-13 catalysts from Figure 6 were selected as model materials. The model Z₂Cu catalyst was a Si/Al = 4.5, 3.86 Cu wt % sample with no Cu_xO_y and 100% of the Cu²⁺ as Z₂Cu. The model ZCuOH catalyst was a Si/Al = 25, 1.50 Cu wt % sample with no Cu_xO_y and 80% of the Cu²⁺ as ZCuOH with the remaining 20% as Z₂Cu. The model Cu_xO_y catalyst was a Si/Al = 4.5, 7.43 wt % sample where an estimated 70% of the Cu speciated as extraframework Cu_xO_y, with the remaining 30% as Z₂Cu. All of these properties are summarized in Table 1. Cu speciation fractions

Table 1. Fraction of Cu species on Cu_xO_y, Z₂Cu, and ZCuOH Model Materials

model material	Si/Al	Cu wt %	fraction Z ₂ Cu	fraction ZCuOH	fraction Cu _x O _y ^a
Cu _x O _y	4.5	7.4	0.3	0.0	0.7
Z ₂ Cu	4.5	3.9	1.0	0.0	0.0
ZCuOH	25	1.5	0.2	0.8	0.0

^aThe fraction of Cu_xO_y sites was calculated from differential SCR rates. The ratio of the actual measured SCR rate on the material with Cu_xO_y to the expected SCR rate assuming that all its Cu were Z₂Cu was used to estimate the fraction of Cu_xO_y.

on our Z₂Cu and ZCuOH model materials were experimentally confirmed using the selective NH₃ titration of the Brønsted acid method reported by Paolucci et al.²² (Figure S4). The fraction of Cu_xO_y was estimated from SCR reaction rates as the ratio of the predicted SCR rate (if all Cu were SCR active) to the experimentally measured reaction rate, as shown in eq 7. The turnover frequency (TOF) (in units of mols of NO per second per mol Cu) is determined from the slope between Cu wt % of 0 and 4 in Figure 6A. The molecular mass of Cu (MW_{Cu}) and Cu wt % were used to convert the TOF to a standard SCR rate per gram catalyst, consistent with the experimentally measured rate. With this formulation, we assume that the active Cu²⁺ centers are captured from our measured SCR rates, and the remaining Cu are inactive Cu_xO_y and pore-blocked Cu²⁺.

$$\begin{aligned} \text{fraction Cu}_{x}\text{O}_{y} &= \frac{r_{\text{if all Cu active}} - r_{\text{experimentally measured}}}{r_{\text{if all Cu active}}} \\ &= \frac{(\text{TOF}) \cdot (\text{MW}_{\text{Cu}}) \cdot (\text{Cu wt \%}) - r_{\text{experimentally measured}}}{(\text{TOF}) \cdot (\text{MW}_{\text{Cu}}) \cdot (\text{Cu wt \%})} \end{aligned} \quad (7)$$

Figure 7 displays Arrhenius plots of the three model materials for standard SCR and N₂O formation. Apparent activation energies and reaction rates of SCR and N₂O formation in addition to the ratio between the N₂O rate and SCR rate are tabulated in Table 2. N₂O formation rates on a per Cu basis are the fastest on ZCuOH, followed by Z₂Cu and then extraframework Cu_xO_y; ZCuOH exhibit N₂O formation rates 11 times faster than Cu_xO_y, and Z₂Cu exhibit N₂O formation rates 2 times faster than Cu_xO_y. Since Cu_xO_y is likely to exist as extraframework nanoparticles (Figure 5), a large fraction of the Cu within the nanoparticles would be shielded from the reaction environment and not directly participate in the catalysis. Relative to the SCR rate, the nonselective N₂O formation rate during standard SCR at 423 K is 8 times higher on ZCuOH than on Z₂Cu. Taken together, these results indicate that although both ZCuOH and Z₂Cu exhibit identical turnover rates normalized per Cu²⁺, commercial Cu-SSZ-13 formulations that minimize or eliminate ZCuOH sites would be beneficial in decreasing N₂O emissions.

Furthermore, we observe no significant difference between the standard SCR apparent activation energies and N₂O formation activation energies. This indicates that the N₂O formation pathway is directly related to SCR and is likely an offshoot of the standard SCR mechanism. We postulate that since the rate-limiting step of SCR is the reduction half-cycle (as indicated by apparent activation energies of ~ 70 kJ mol⁻¹), N₂O formation is linked to the reduction half-cycle on both ZCuOH and Z₂Cu active centers. This experimental observation is consistent with recent results by Xi et al.,⁴⁶ where they observed an increase in N₂O with an increase in the number of reducible Cu quantified from a reductive mixture of NO + NH₃.

We also note that our kinetic results do not clarify the effect of extraframework Cu_xO_y, nor does it rule out the possibility of N₂O formation over other ammonium nitrate intermediates in the oxidation half-cycle. To clarify the effect of extraframework Cu_xO_y species, a better model catalyst would involve the Cu-exchange of pure Si (Si/Al = ∞) Cu-SSZ-13 using the ion-exchange Cu(OH)₂ precipitation route at high pH discussed earlier, free of Z₂Cu and ZH species.

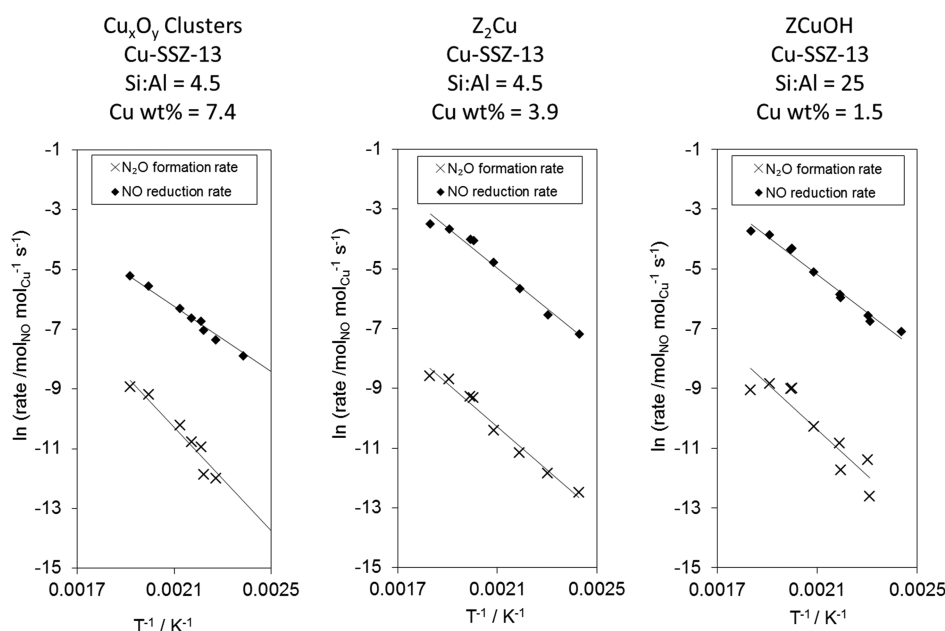


Figure 7. Arrhenius plots of the SCR NO reduction rate (black diamonds) and the N_2O formation rate during SCR (black crosses) on model Cu_xO_y , Z_2Cu , and $ZCuOH$ Cu-SSZ-13. Standard SCR conditions were used (300 ppm NH_3 , 300 ppm NO, 10% O_2 , 8% CO_2 , 2.5% H_2O , and balance N_2 , 423–523 K).

Table 2. Standard SCR Reaction Rates and Apparent Activation Energies Compared to the N_2O Formation Rates and Activation Energies on Cu_xO_y , Z_2Cu , and $ZCuOH$ Model Materials (All Reported at 473 K, Interpolated from Rates Collected between 423 and 523 K)^a

model catalyst	Cu wt %	SCR E_{app} (kJ mol ⁻¹)	SCR rate (mol _{NO} mol _{Cu} ⁻¹ s ⁻¹)	N_2O E_{app} (kJ mol ⁻¹)	N_2O rate (mol _{N₂O} mol _{Cu} ⁻¹ s ⁻¹)	rate _{N₂O} :rate _{SCR}
Cu_xO_y	7.43	58	1.8×10^{-3}	76	3.0×10^{-5}	0.017
Z_2Cu	3.86	63	6.9×10^{-3}	60	5.6×10^{-5}	0.008
$ZCuOH$	1.50	58	5.1×10^{-3}	64	3.4×10^{-4}	0.067

^aThe ratio of the N_2O formation rate and standard SCR rate is tabulated in the right-most column. Errors (2 times the standard deviation) for apparent activation energies are ~ 8 kJ mol⁻¹.

To explore whether N_2O formation occurs via an offshoot from the oxidation half-cycle, we utilized sulfur-poisoned Z_2Cu and $ZCuOH$ samples from Shih et al.¹⁴ Shih et al. observed a decrease in the SCR apparent activation energy with increasing sulfur poisons on the $ZCuOH$ model catalyst concurrent with an increase in the *operando* steady-state Cu(I) fraction¹⁴ and interpreted it as a shift in the SCR rate-limiting step from reduction-limited to oxidation-limited.³⁴ We predict that if the N_2O formation apparent activation energy decreases with decreasing SCR apparent activation energy, the N_2O formation would indeed also occur in the oxidation half-cycle. If the N_2O formation apparent activation energy remains unchanged with decreasing standard SCR apparent activation energy, then we would postulate that it indicates that N_2O formation mechanistically occurs as an offshoot from the reduction half-cycle.

Figure 8 plots the SCR apparent activation energy (filled shapes) and the N_2O formation apparent activation energies (hollow shapes) on model Z_2Cu (triangles) and $ZCuOH$ (diamonds) Cu-SSZ-13. We first observe on Z_2Cu that increasing sulfur poisoning does not induce a decrease in the standard SCR apparent activation energy or N_2O formation activation energy. Because of the unchanged apparent activation energies, we are unable to determine whether N_2O formation can occur in the oxidation half-cycle on Z_2Cu sites. On the other hand, for $ZCuOH$, as the standard SCR apparent

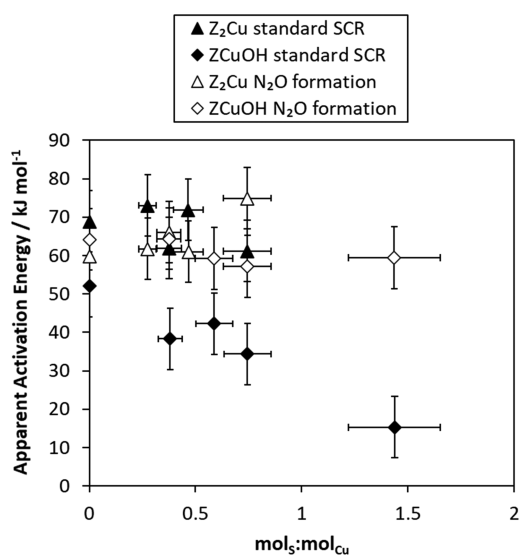


Figure 8. N_2O formation apparent activation energy does not change within error with increasing sulfur poisoning on both model Z_2Cu (hollow triangles) and $ZCuOH$ (hollow diamonds) Cu-SSZ-13 materials. The standard SCR apparent activation energy decreases with increasing sulfur poisoning on $ZCuOH$ model Cu-SSZ-13 (solid diamonds) but does not change with increasing sulfur poisoning on Z_2Cu model Cu-SSZ-13 (solid triangles).

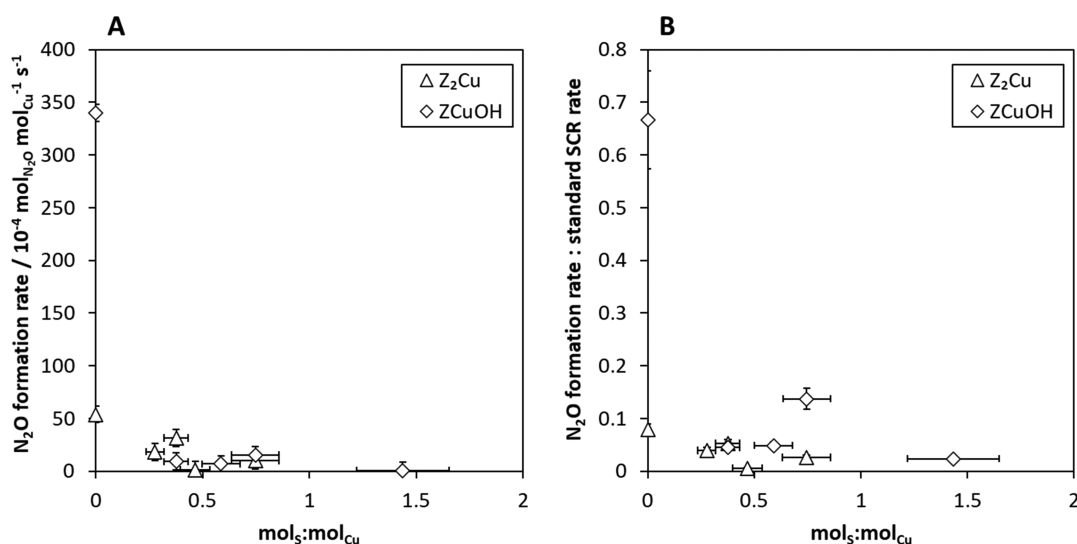


Figure 9. (A) N₂O formation rate over Z₂Cu (hollow triangles) and ZCuOH (hollow diamonds) Cu-SSZ-13 catalysts before and after sulfur poisoning and after desulfation. The presence of sulfation suppresses the N₂O formation rate with ZCuOH exhibiting the largest decrease in N₂O formation after sulfur poisoning. (B) Although the presence of sulfur suppresses both the standard SCR and N₂O formation rate, the N₂O formation rate is suppressed to greater extents than the standard SCR rate after sulfation and desulfation on the ZCuOH Cu-SSZ-13 (diamonds). Sulfation suppresses the N₂O formation rate and standard SCR rate by approximately equal extents on Z₂Cu Cu-SSZ-13 (triangles).

activation energy decreased with increasing sulfur poisons, the N₂O formation apparent activation energy remained constant. Taken together, we rule out the possibility of N₂O formation during the reoxidation of Cu(NH₃)₂⁺ on ZCuOH but were unable to rule out the possibility of N₂O formation during the oxidation half-cycle on Z₂Cu.

In addition to apparent activation energies, the effects of sulfur poisons on the N₂O formation rate and selectivity on ZCuOH and Z₂Cu were also studied. The N₂O formation rate normalized per Cu plotted versus molar S/Cu ratio (Figure 9A) shows that an increase in S/Cu suppresses the N₂O formation rate on both ZCuOH and Z₂Cu model catalysts, with the rate suppressed on ZCuOH by a factor of ~17 times as compared to a suppression of ~2 times on Z₂Cu. Because sulfur poisons also decrease the SCR rate normalized per Cu, we plot the ratio of the N₂O formation rate to the SCR rate (Figure 9B). If both the N₂O formation rate and SCR rate decreased by the same proportions, we would have measured constant ratios with increasing molar S/Cu. Rather, we observe a 10-fold decrease on ZCuOH and a 2-fold decrease on Z₂Cu active centers. These results indicate that sulfur poisons decrease the N₂O selectivity on both ZCuOH and Z₂Cu active centers, with the highest suppression observed on ZCuOH.

3.2.3. Mechanistic Considerations for N₂O Formation.

Since our experimental apparent activation energy kinetics allude that N₂O formation occurs as an offshoot from the reduction half-cycle, we utilize reaction orders (NH₃, NO, O₂, and H₂O), atom and electron balances, and insights from the literature to piece together a mechanistic map of how N₂O may form during standard SCR.

We observe that N₂O formation reaction orders seem to be zero with respect to NH₃, O₂, and H₂O and first order with respect to NO, albeit with high experimental errors (Figure 10 and Table 3). Due to the large errors, these results must be taken with care. These high errors are due to the concentration of N₂O impinging at or near the detection limit of an MKS Multigas 2030 gas-phase FTIR spectrometer. If we take the experimental N₂O formation reaction orders at face value on

both Z₂Cu and ZCuOH, NO orders of ~1 and O₂ orders of ~0 are consistent with N₂O stemming from the reduction half-cycle and not the oxidation half-cycle. Xi et al.⁴⁶ experimentally observed an increase in the N₂O formation rate with increasing NO concentration from 0 to ~500 ppm and a subsequent decrease in the N₂O formation rate at NO concentrations higher than ~500 ppm. In comparison, we observe an increase in the N₂O formation rate at NO concentrations up to 1000 ppm. At NO concentrations greater than ~500 ppm, we do observe a rise in NO₂ leaving the catalyst bed with increasing NO concentrations (Figure S21), indicating that in addition to standard SCR and N₂O formation, NO₂ formation (presumably from NO oxidation) becomes more prevalent with increasing NO concentrations. This NO₂, if present at high enough concentrations, may affect the N₂O formation rate by activating the ammonium nitrate decomposition route. On ZCuOH sites, however, due to the large uncertainty in the O₂ order, it is still possible that N₂O formation can occur in the oxidation half-cycle, perhaps via a mechanism proposed by Feng et al.⁴⁷ where the decomposition of H₂NNO species over Cu-OOH-Cu was found to be energetically favorable relative to the decomposition of ammonium nitrate. This can still be consistent with the observed apparent activation energies in the previous section if N₂O formation during the oxidation half-cycle contributes to only a minor fraction of the total N₂O.

As discussed in the Introduction, the formation of N₂O has been proposed to occur from the decomposition of ammonium nitrate (NH₄NO₃);^{38–43} however, many of the studies that observed and proposed NH₄NO₃ as an intermediate utilized NO₂ as an oxidant. Xi et al.⁴⁶ did not observe the presence of nitrates from *in situ* DRIFTS in the absence of NO₂, which indicates that no NH₄NO₃ is formed, or if formed, nitrates are a short-lived intermediate. Although the concentration of NO₂ in the standard SCR-simulated exhaust is ideally 0, in reality during our experiments, the NO₂ concentration is typically between 1 and 2 ppm (Figure S21). This low concentration is present as an impurity in our NO cylinder and can also form from gas-phase NO oxidation,³⁴ NO oxidation in zeolite

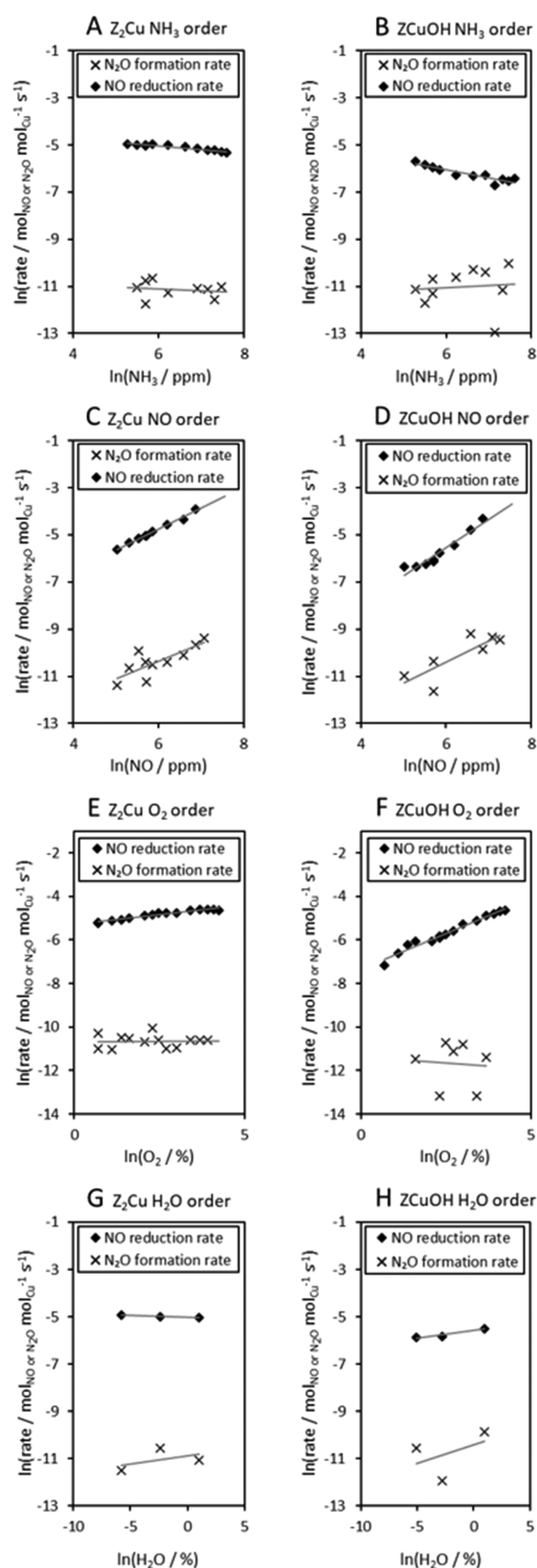


Figure 10. Apparent reaction order plots for NH_3 (between 150 and 2000 ppm), NO (between 150 and 1000 ppm), O_2 (between 1 and 60%), and H_2O (between 10–5 and 2.5%) for standard SCR (black diamonds) and N_2O formation (black crosses) on the Z_2Cu model material (Cu-SSZ-13, Si/Al = 4.5, Cu wt % = 3.9) and ZCuOH model material (Cu-SSZ-13, Si/Al = 25, Cu wt % = 1.5). The slope of the log–log plot is the apparent reaction order, summarized in Table 3.

voids,⁹⁹ and/or over extraframework Cu_xO_y .⁸¹ Because the formation rate of N_2O is an order of magnitude higher than the rate of NO_2 entering the reactor, we believe that the NO_2 pathway does not significantly contribute to the N_2O formed during standard SCR—unless there is additional NO_2 being formed within the reactor system and consumed prior to the downstream FTIR detector.

From atomic balances, nitrosoamide (NH_2NO) and ammonium nitrite (NH_4NO_2) intermediates require one additional oxygen atom to stoichiometrically decompose into N_2O and H_2O . All possible sources of oxygen atoms include: O from the zeolite lattice, O from O_2 , O from NO , O from H_2O , and O from NO_2 . Because increasing the H_2O pressures has been shown to increase N_2O selectivity^{45,56,57} in the literature, it is possible that H_2O is an O source. In particular, Liu et al.⁵⁷ observed an increase in N_2O formation with increasing H_2O concentrations up to 2%, and a subsequent decrease in N_2O formation with higher H_2O concentrations at 523 K. This is consistent with our experimentally measured H_2O orders (only between 0 and 2.5% H_2O); H_2O has a slightly positive reaction order but with high errors—providing not enough certainty to rule out the role of H_2O . Wang et al. (on $\text{MnO}_x/\text{TiO}_2$)⁶³ and Chen et al. (on Cu-SSZ-13)⁴⁰ have demonstrated that the two N atoms in N_2O originate from NO and NH_3 , one N atom from each. They also further demonstrated that O from the framework support and O from O_2 can contribute to N_2O formation. Our experimentally measured O_2 orders seem to indicate that O_2 pressure does not contribute to N_2O formation kinetics; however, there is not enough certainty to rule out the role of O_2 in providing O to form N_2O under standard SCR conditions on Cu-SSZ-13. From these studies, these possible sources of O are added as a possible mechanistic pathway to Figure 11.

As summarized in Figure 11, the standard SCR reduction half-cycle (pathway with black arrows) is the dominant pathway where $\text{Cu}(\text{NH}_3)_4^{2+}$ and $\text{Cu}(\text{NH}_3)\text{OH}^+$ active centers form nitrosoamide (NH_2NO) and ammonium nitrite (NH_4NO_2) intermediates upon reaction with NO , respectively. These intermediates can then dissociate via the standard SCR pathway to produce $\text{Cu}(\text{NH}_3)_2^+$, N_2 , and H_2O ^{22,26–28} through a cascade of electron transfers and bond rearrangements. If an additional oxygen atom is provided, the nitrosoamide (NH_2NO) and ammonium nitrite (NH_4NO_2) intermediates can then produce $\text{Cu}(\text{NH}_3)_2^+$, N_2O , and H_2O as an offshoot from the reduction half-cycle. A parallel pathway that involves NO_2 is also included in Figure 11 however, it is improbable that this pathway will occur to any significant extent during standard SCR.

4. CONCLUSIONS

We first demonstrated that the $\text{Cu}(\text{NO}_3)_2$ molarity and pH are two factors that can be utilized to control the precipitation of $\text{Cu}(\text{OH})_2$ species during aqueous Cu-exchange of zeolites. Upon calcination, $\text{Cu}(\text{OH})_2$ is oxidized to extraframework Cu_xO_y species as evidenced by UV–visible and XRD characterization. We then demonstrated that extraframework Cu_xO_y species are detrimental toward standard SCR and deduce from unchanged apparent activation energies that the transport of SCR reactants and products to/from the remaining Cu^{2+} active centers are unaffected by the presence of Cu_xO_y .

Table 3. Summary of Kinetic Parameters from the Power-Law Rate (Equation 4) for Standard SCR and N₂O Formation^a

kinetic parameter	Z ₂ Cu		ZCuOH	
	standard SCR	N ₂ O formation	standard SCR	N ₂ O formation
$E_{a,apparent}$ (kJ mol ⁻¹)	58 ± 8	64 ± 8	63 ± 8	60 ± 8
NH ₃ order	-0.15 ± 0.04	-0.07 ± 0.33	-0.34 ± 0.09	0.16 ± 0.80
NO order	0.88 ± 0.07	0.74 ± 0.41	0.85 ± 0.29	0.89 ± 0.56
O ₂ order	0.18 ± 0.02	0.01 ± 0.16	0.66 ± 0.06	-0.12 ± 0.67
H ₂ O order	-0.01 ± 0.02	0.07 ± 0.25	0.07 ± 0.10	0.16 ± 0.61

^aReported errors are 2 times the standard deviation, which covers ~95% of the scatter.

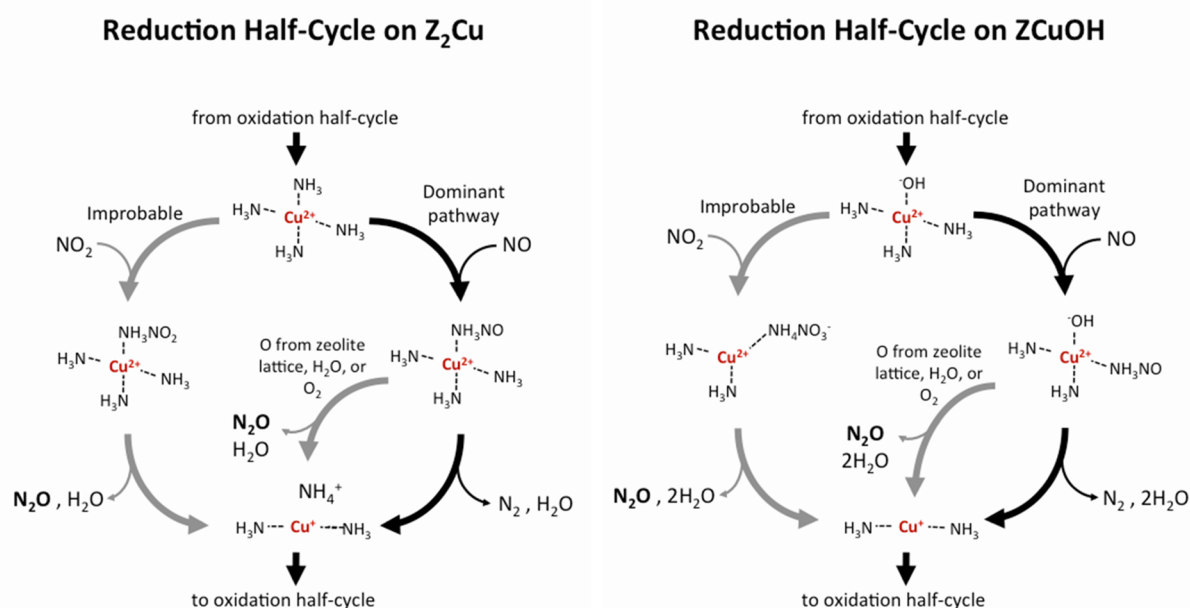


Figure 11. Proposed reduction half-cycle mechanism on Z₂Cu (left) and ZCuOH (right) by the dominant standard SCR pathway represented by the black arrows. The gray arrows represent deviations from this dominant pathway where the formation of undesirable N₂O can occur.

Utilizing model ZCuOH, Z₂Cu, and Cu_xO_y Cu-SSZ-13 catalysts, the effects of Cu speciation on N₂O formation rates and kinetics were studied. Our findings indicated that the N₂O formation rates on a per Cu basis were the fastest on ZCuOH sites by an order magnitude than the next fastest Z₂Cu and the slowest on Cu_xO_y sites. Because N₂O formation apparent activation energies were indistinguishable from the standard SCR reduction rate-limiting apparent activation energies, we postulated that N₂O formation stems as an offshoot from the reduction-limited half-cycle. This postulate was further supported from sulfur poisoning experiments on ZCuOH where the N₂O formation apparent activation energy remained constant while the standard SCR apparent activation energy decreased with increasing sulfur poisons. The decrease in the activation energy is interpreted as a shift from reduction-limited kinetics to oxidation-limited kinetics induced by a decrease in the active Cu density caused by the sulfur poisons. These fundamental insights about the underlying mechanism for N₂O formation offer potential toward designing new SCR catalysts with uncompromised NO_x conversion and lower N₂O formation.

■ ASSOCIATED CONTENT

SI Supporting Information

The Supporting Information is available free of charge at <https://pubs.acs.org/doi/10.1021/acscatal.1c01871>.

Reactor rig flow diagram and example kinetic measurements (Section S1); NH₃ titration results of Z₂Cu and ZCuOH model catalysts (Section S2); Cu(OH)₂ precipitation equilibrium constant (K_{sp}) derivation (Section S3); precipitation curves of Cu(CH₃COO)₂ and CuSO₄ (Section S4); formation of Cu_xO_y species in Cu-ZSM-5 and Cu-β zeolites after aqueous Cu-exchange in Cu(NO₃)₂ and subsequent calcination (Section S5); UV-visible characterization of Cu-SSZ-13 (Section S6); XRD characterization of Cu-SSZ-13 (Section S7); deactivation of anionic sites during low pH aqueous Cu-exchange (Section S8); kinetics of SCR and N₂O formation (Section S9); error propagation equations (Section S10); and references (Section S11) (PDF)

■ AUTHOR INFORMATION

Corresponding Authors

Arthur J. Shih – Charles D. Davidson School of Chemical Engineering, Purdue University, West Lafayette, Indiana 47907, United States; Leiden Institute of Chemistry, Leiden University, 2300 RA Leiden, The Netherlands; orcid.org/0000-0002-2414-0644; Email: a.j.shih@lic.leidenuniv.nl

Aida Luz Villa – Environmental Catalysis Research Group, Chemical Engineering Department, Engineering Faculty, Universidad de Antioquia, Medellín 050010, Colombia;

orcid.org/0000-0002-3770-3223; Email: aida.villa@udea.edu.co

Authors

Juan M. González – Charles D. Davidson School of Chemical Engineering, Purdue University, West Lafayette, Indiana 47907, United States; Environmental Catalysis Research Group, Chemical Engineering Department, Engineering Faculty, Universidad de Antioquia, Medellín 050010, Colombia

Ishant Khurana – Charles D. Davidson School of Chemical Engineering, Purdue University, West Lafayette, Indiana 47907, United States; orcid.org/0000-0002-5444-0103

Lucía Pérez Ramírez – Charles D. Davidson School of Chemical Engineering, Purdue University, West Lafayette, Indiana 47907, United States

Andres Peña L. – Charles D. Davidson School of Chemical Engineering, Purdue University, West Lafayette, Indiana 47907, United States

Ashok Kumar – Cummins Inc., Columbus, Indiana 47201, United States

Complete contact information is available at:
<https://pubs.acs.org/10.1021/acscatal.1c01871>

Notes

The authors declare no competing financial interest.

ACKNOWLEDGMENTS

The authors acknowledge Dr. Aleksey Yezerets, Dr. Krishna Kamasamudram, and the researchers in the Cummins Catalyst Technology Team. The authors also acknowledge financial support provided by the National Science Foundation GOALI program under award number 1258715-CBET (Purdue), the U.S. Department of Energy Vehicle Technologies Program under contract number DE-EE0003977 and by Cummins, Inc. We thank Sachem, Inc., for providing the organic structure-directing agent used to synthesize SSZ-13. J.M.G. and A.L.V. acknowledge the Universidad de Antioquia and funding from the Purdue Colombia Initiative. J.M.G., L.P.R., A.P.L., and A.L.V. contributed as part of mobility programs coordinated by the Colombia Purdue Partnership.

REFERENCES

- (1) Iwamoto, M.; Yahiro, H.; Yu-u, Y.; Shundo, S.; Mizuno, N. *Shokubai* **1990**, *32*, 430.
- (2) Held, W.; König, A.; Richter, T.; Puppe, L. Catalytic NO_x Reduction in Net Oxidizing Exhaust Gas. *SAE Tech. Pap. Ser.* **1990**, *99*, 209–216.
- (3) Bull, I.; Xue, W.; Burk, P.; Boorse, R. S.; Jaglowski, W. M.; Koermer, G. S.; Moini, A.; Patchett, J. A.; Dettling, J. C.; Claude, M. T. U.S. Patent US7,601,662 B2, 2009.
- (4) Wang, A.; Olsson, L. The Impact of Automotive Catalysis on the United Nations Sustainable Development Goals. *Nat. Catal.* **2019**, *2*, 566–570.
- (5) Lambert, C. K. Current State of the Art and Future Needs for Automotive Exhaust Catalysis. *Nat. Catal.* **2019**, *2*, 554–557.
- (6) Wallington, T. J.; Wiesen, P. N₂O Emissions from Global Transportation. *Atmos. Environ.* **2014**, *94*, 258–263.
- (7) *Overview of Greenhouse Gases*; United States Environmental Protection Agency, 2018.
- (8) *Inventory of U.S. Greenhouse Gas Emissions and Sinks 1990–2016*; United States Environmental Protection Agency, 2018.
- (9) Pérez-Ramírez, J.; Kapteijn, F.; Schöffel, K.; Moulijn, J. A. Formation and Control of N₂O in Nitric Acid Production Where Do We Stand Today? *Appl. Catal., B* **2003**, *44*, 117–151.

(10) Tian, H.; Xu, R.; Canadell, J. G.; Thompson, R. L.; Winiwarter, W.; Suntharalingam, P.; Davidson, E. A.; Ciais, P.; Jackson, R. B.; Janssens-Maenhout, G.; Prather, M. J.; Regnier, P.; Pan, N.; Pan, S.; Peters, G. P.; Shi, H.; Tubiello, F. N.; Zaehle, S.; Zhou, F.; Arneeth, A.; Battaglia, G.; Berthet, S.; Bopp, L.; Bouwman, A. F.; Buitenhuis, E. T.; Chang, J.; Chipperfield, M. P.; Dangal, S. R. S.; Dlugokencky, E.; Elkins, J. W.; Eyre, B. D.; Fu, B.; Hall, B.; Ito, A.; Joos, F.; Krummel, P. B.; Landolfi, A.; Laruelle, G. G.; Lauerwald, R.; Li, W.; Lienert, S.; Maavara, T.; Macleod, M.; Millet, D. B.; Olin, S.; Patra, P. K.; Prinn, R. G.; Raymond, P. A.; Ruiz, D. J.; Werf, G. R.; Vuichard, N.; Wang, J.; Weiss, R. F.; Wells, K. C.; Wilson, C.; Yang, J.; Yao, Y. A Comprehensive Quantification of Global Nitrous Oxide Sources and Sinks. *Nature* **2020**, *586*, 248–256.

(11) Luo, J.; Wang, D.; Kumar, A.; Kamasamudram, K.; Currier, N.; Yezerets, A. Identification of Two Types of Cu Sites and Their Unique Responses to Hydrothermal Aging and Sulfur Poisoning. *Catal. Today* **2016**, *267*, 3–9.

(12) Jangjou, Y.; Do, Q.; Gu, Y.; Lim, L. G.; Sun, H.; Wang, D.; Kumar, A.; Li, J.; Grabow, L. C.; Epling, W. S. Nature of Cu Active Centers in Cu-SSZ-13 and Their Responses to SO₂ Exposure. *ACS Catal.* **2018**, *8*, 1325–1337.

(13) Hammershøi, P. S.; Jangjou, Y.; Epling, W. S.; Jensen, A. D.; Janssens, T. V. W. Reversible and Irreversible Deactivation of Cu-CHA NH₃-SCR Catalysts by SO₂ and SO₃. *Appl. Catal., B* **2018**, *226*, 38–45.

(14) Shih, A. J.; Khurana, I.; Li, H.; González, J.; Kumar, A.; Paolucci, C.; Lardinois, T. M.; Jones, C. B.; Albarracín Caballero, J. D.; Kamasamudram, K.; Yezerets, A.; Delgass, W. N.; Miller, J. T.; Villa, A. L.; Schneider, W. F.; Gounder, R.; Ribeiro, F. H. Spectroscopic and Kinetic Responses of Cu-SSZ-13 to SO₂ Exposure and Implications for NO_x Selective Catalytic Reduction. *Appl. Catal., A* **2019**, *574*, 122–131.

(15) Wang, A.; Xie, K.; Bernin, D.; Kumar, A.; Kamasamudram, K.; Olsson, L. Deactivation Mechanism of Cu Active Sites in Cu/SSZ-13 - Phosphorus Poisoning and the Effect of Hydrothermal Aging. *Appl. Catal., B* **2020**, *269*, No. 118781.

(16) Albarracín-Caballero, J. D.; Khurana, I.; Di Iorio, J. R.; Shih, A. J.; Schmidt, J. E.; Dusselier, M.; Davis, M. E.; Yezerets, A.; Miller, J. T.; Ribeiro, F. H.; Gounder, R. Structural and Kinetic Changes to Small-Pore Cu-Zeolites after Hydrothermal Aging Treatments and Selective Catalytic Reduction of NO_x with Ammonia. *React. Chem. Eng.* **2017**, *2*, 168–179.

(17) Bates, S. A.; Verma, A. A.; Paolucci, C.; Parekh, A. A.; Anggara, T.; Yezerets, A.; Schneider, W. F.; Miller, J. T.; Delgass, W. N.; Ribeiro, F. H. Identification of the Active Cu Site in Standard Selective Catalytic Reduction with Ammonia on Cu-SSZ-13. *J. Catal.* **2014**, *312*, 87–97.

(18) Boudart, M. Turnover Rates in Heterogeneous Catalysis. *Chem. Rev.* **1995**, *95*, 661–666.

(19) Korhonen, S. T.; Fickel, D. W.; Lobo, R. F.; Weckhuysen, M.; Beale, A. M. Isolated Cu²⁺ Ions: Active Sites for Selective Catalytic Reduction of NO. *Chem. Commun.* **2011**, *47*, 800–802.

(20) Kwak, J. H.; Zhu, H.; Lee, J. H.; Peden, C. H. F.; Szanyi, J. Two Different Cationic Positions in Cu-SSZ-13? *Chem. Commun.* **2012**, *48*, 4758–4760.

(21) Borfecchia, E.; Lomachenko, K. A.; Giordanino, F.; Falsig, H.; Beato, P.; Soldatov, A. V.; Bordiga, S.; Lamberti, C. Revisiting the Nature of Cu Sites in the Activated Cu-SSZ-13 Catalyst for SCR Reaction. *Chem. Sci.* **2015**, *6*, 548–563.

(22) Paolucci, C.; Parekh, A. A.; Khurana, I.; Di Iorio, J. R.; Li, H.; Albarracín Caballero, J. D.; Shih, A. J.; Anggara, T.; Delgass, W. N.; Miller, J. T.; Ribeiro, F. H.; Gounder, R.; Schneider, W. F. Catalysis in a Cage: Condition-Dependent Speciation and Dynamics of Exchanged Cu Cations in SSZ-13 Zeolites. *J. Am. Chem. Soc.* **2016**, *138*, 6028–6048.

(23) Di Iorio, J. R.; Gounder, R. Controlling the Isolation and Pairing of Aluminum in Chabazite Zeolites Using Mixtures of Organic and Inorganic Structure-Directing Agents. *Chem. Mater.* **2016**, *28*, 2236–2247.

- (24) Kispersky, V. F.; Kropf, A. J.; Ribeiro, F. H.; Miller, J. T. Low Absorption Vitreous Carbon Reactors for Operando XAS: A Case Study on Cu/Zeolites for Selective Catalytic Reduction of NO_x by NH₃. *Phys. Chem. Chem. Phys.* **2012**, *14*, 2229–2238.
- (25) Paolucci, C.; Khurana, I.; Parekh, A. A.; Li, S.; Shih, A. J.; Li, H.; Di Iorio, J. R.; Albarracin-Caballero, J. D.; Yezerets, A.; Miller, J. T.; Delgass, W. N.; Ribeiro, F. H.; Schneider, W. F.; Gounder, R. Dynamic Multinuclear Sites Formed by Mobilized Copper Ions in NO_x Selective Catalytic Reduction. *Science* **2017**, *357*, 898–903.
- (26) Paolucci, C.; Verma, A. A.; Bates, S. A.; Kispersky, V. F.; Miller, J. T.; Gounder, R.; Delgass, W. N.; Ribeiro, F. H.; Schneider, W. F. Isolation of the Copper Redox Steps in the Standard Selective Catalytic Reduction on Cu-SSZ-13. *Angew. Chem., Int. Ed.* **2014**, *53*, 1–7.
- (27) Greenaway, A. G.; Marberger, A.; Thetford, A.; Catlow, C. R. A.; Beale, A. M.; et al. Detection of key transient Cu intermediates in SSZ-13 during NH₃-SCR deNO_x by modulation excitation IR spectroscopy. *Chem. Sci.* **2020**, *11*, 447–455.
- (28) Janssens, T. V. W.; Falsig, H.; Lundegaard, L. F.; Vennestrom, P. N. R.; Rasmussen, S.; Moses, P. G.; Giordanino, F.; Borfecchia, E.; Lomachenko, K.; Lamberti, C.; Bordiga, S.; Godiksen, A.; Mossin, S.; Beato, P. A Consistent Reaction Scheme for the Selective Catalytic Reduction of Nitrogen Oxides with Ammonia. *ACS Catal.* **2015**, No. 150319102200004.
- (29) Gramigni, F.; Nasello, N. D.; Usberti, N.; Iacobone, U.; Selleri, T.; Hu, W.; Liu, S.; Gao, X.; Nova, I.; Tronconi, E. Transient Kinetic Analysis of Low-Temperature NH₃-SCR over Cu-CHA Catalysts Reveals a Quadratic Dependence of Cu Reduction Rates on Cu^{II}. *ACS Catal.* **2021**, *11*, 4821–4831.
- (30) Gao, F.; Mei, D.; Wang, Y.; Szanyi, J.; Peden, C. H. F. Selective Catalytic Reduction over Cu/SSZ-13: Linking Homo- and Heterogeneous Catalysis. *J. Am. Chem. Soc.* **2017**, *139*, 4935–4942.
- (31) Chen, L.; Falsig, H.; Janssens, T. V. W.; Jansson, J.; Skoglundh, M.; Grönbeck, H. Effect of Al-Distribution on Oxygen Activation over Cu-CHA. *Catal. Sci. Technol.* **2018**, *8*, 2131–2136.
- (32) Chen, L.; Falsig, H.; Janssens, T. V. W.; Grönbeck, H. Activation of Oxygen on (NH₃-Cu-NH₃)⁺ in NH₃-SCR over Cu-CHA. *J. Catal.* **2018**, *358*, 179–186.
- (33) Chen, L.; Janssens, T. V. W.; Vennestrom, P. N. R.; Jansson, J.; Skoglundh, M.; Grönbeck, H. A Complete Multisite Reaction Mechanism for Low-Temperature NH₃-SCR over Cu-CHA. *ACS Catal.* **2020**, *10*, 5646–5656.
- (34) Jones, C. B.; Khurana, I.; Krishna, S. H.; Shih, A. J.; Delgass, W. N.; Miller, J. T.; Ribeiro, F. H.; Schneider, W. F.; Gounder, R. Effects of Dioxygen Pressure on Rates of NO_x Selective Catalytic Reduction with NH₃ on Cu-CHA Zeolites. *J. Catal.* **2020**, *389*, 140–149.
- (35) Kamasamudram, K.; Henry, C.; Currier, N.; Yezerets, A. N₂O Formation and Mitigation in Diesel Aftertreatment Systems. *SAE Int. J. Engines* **2012**, *5*, 688–698.
- (36) Bartley, G. J.; Sharp, C. A. Brief Investigation of SCR High Temperature N₂O Production. *SAE Int. J. Engines* **2012**, *5*, 683–687.
- (37) Akter, N.; Chen, X.; Parise, J.; Boscoboinik, J. A.; Kim, T. Effects of Copper Loading on NH₃-SCR and NO Oxidation over Cu Impregnated CHA Zeolite. *Korean J. Chem. Eng.* **2017**, *34*, 1–10.
- (38) Luo, J.; Gao, F.; Kamasamudram, K.; Currier, N.; Peden, C. H. F.; Yezerets, A. New Insights into Cu/SSZ-13 SCR Catalyst Acidity. Part I: Nature of Acidic Sites Probed by NH₃ Titration. *J. Catal.* **2017**, *348*, 291–299.
- (39) Ottinger, N.; Xi, Y.; Keturakis, C.; Liu, Z. G. Impact of Hydrothermal Aging on the Formation and Decomposition of Ammonium Nitrate on a Cu/Zeolite SCR Catalyst. *SAE Int. J. Engines* **2017**, *10*, 1646–1652.
- (40) Chen, H.-Y.; Wei, Z.; Kollar, M.; Gao, F.; Wang, Y.; Szanyi, J.; Peden, C. H. F. A Comparative Study of N₂O Formation during the Selective Catalytic Reduction of NO_x with NH₃ on Zeolite Supported Cu Catalysts. *J. Catal.* **2015**, *329*, 490–498.
- (41) Cui, Y.; Gao, F. Cu Loading Dependence of Fast NH₃-SCR on Cu/SSZ-13. *Emiss. Control Sci. Technol.* **2019**, *5*, 124–132.
- (42) Xie, L.; Liu, F.; Liu, K.; Shi, X.; He, H. Inhibitory Effect of NO₂ on the Selective Catalytic Reduction of NO_x with NH₃ over One-Pot-Synthesized Cu-SSZ-13 Catalyst. *Catal. Sci. Technol.* **2014**, *4*, 1104.
- (43) Luo, J.; Tang, Y.; Joshi, S.; Kamasamudram, K.; Currier, N.; Yezerets, A. The Impact of Ammonium Nitrate Species on Low Temperature NO_x Conversion Over Cu/CHA SCR Catalyst. *SAE Int. J. Engines* **2017**, *10*, 1691–1696.
- (44) Colombo, M.; Nova, I.; Tronconi, E. A Comparative Study of the NH₃-SCR Reactions over a Cu-Zeolite and a Fe-Zeolite Catalyst. *Catal. Today* **2010**, *151*, 223–230.
- (45) Zhang, D.; Yang, R. T. N₂O Formation Pathways over Zeolite-Supported Cu and Fe Catalysts in NH₃-SCR. *Energy Fuels* **2018**, *32*, 2170–2182.
- (46) Xi, Y.; Ottinger, N. A.; Keturakis, C. J.; Liu, Z. G. Dynamics of Low Temperature N₂O Formation under SCR Reaction Conditions over a Cu-SSZ-13 Catalyst. *Appl. Catal., B* **2021**, *294*, No. 120245.
- (47) Feng, Y.; Janssens, T. V. W.; Vennestrom, P. N. R.; Jansson, J.; Skoglundh, M.; Grönbeck, H. The Role of H⁺ - and Cu⁺ - Sites for N₂O Formation during NH₃-SCR over Cu-CHA. *J. Phys. Chem. C* **2021**, *125*, 4595–4601.
- (48) Shan, Y.; Shi, X.; He, G.; Liu, K.; Yan, Z.; Yu, Y.; He, H. Effects of NO₂ Addition on the NH₃-SCR over Small-Pore Cu-SSZ-13 Zeolites with Varying Cu Loadings. *J. Phys. Chem. C* **2018**, *122*, 25948–25953.
- (49) Kwak, J. H.; Tran, D.; Szanyi, J.; Peden, C. H. F.; Lee, J. H. The Effect of Copper Loading on the Selective Catalytic Reduction of Nitric Oxide by Ammonia Over Cu-SSZ-13. *Catal. Lett.* **2012**, *142*, 295–301.
- (50) Li, S.; Zheng, Y.; Gao, F.; Szanyi, J.; Schneider, W. F. Experimental and Computational Interrogation of Fast SCR Mechanism and Active Sites on H-Form SSZ-13. *ACS Catal.* **2017**, *7*, 5087–5096.
- (51) Goncalves, T. J.; Plessow, P. N.; Studt, F. Theoretical Study on the NO_x Selective Catalytic Reduction on Single-Cu Sites and Brønsted Acid Sites in Cu-SSZ-13. *J. Phys. Chem. C* **2021**, *125*, 12594–12602.
- (52) Kumar, A.; Kamasamudram, K.; Currier, N.; Yezerets, A. Effect of Transition Metal Ion Properties on the Catalytic Functions and Sulfation Behavior of Zeolite-Based SCR Catalysts. *SAE Int. J. Engines* **2017**, *10*, No. 9.
- (53) Delahay, G.; Coq, B.; Kieger, S.; Neveu, B. The Origin of N₂O Formation in the Selective Catalytic Reduction of NO by NH₃ in O₂ Rich Atmosphere on Cu-Faujasite Catalysts. *Catal. Today* **1999**, *54*, 431–438.
- (54) Grossale, A.; Nova, I.; Tronconi, E.; Chatterjee, D.; Weibel, M. The Chemistry of the NO/NO₂-NH₃ “Fast” SCR Reaction over Fe-ZSM5 Investigated by Transient Reaction Analysis. *J. Catal.* **2008**, *256*, 312–322.
- (55) Takamitsu, Y.; Ito, Y.; Ogawa, H.; Sano, T. Effect of Oxygen Concentration in NH₃-SCR Reaction over Fe- and Cu-Loaded Beta Zeolites. *J. Jpn. Pet. Inst.* **2012**, *55*, 57–66.
- (56) Tarach, K. A.; Jabłońska, M.; Pyra, K.; Liebau, M.; Reiprich, B.; Gläser, R.; Gora-Marek, K. Effect of Zeolite Topology on NH₃-SCR Activity and Stability of Cu-Exchanged Zeolites. *Appl. Catal., B* **2021**, *284*, No. 119752.
- (57) Liu, B.; Yao, D.; Wu, F.; Wei, L.; Li, X.; Wang, X. Experimental Investigation on N₂O Formation during the Selective Catalytic Reduction of NO_x with NH₃ over Cu-SSZ-13. *Ind. Eng. Chem. Res.* **2019**, *58*, 20516–20527.
- (58) Kubota, H.; Liu, C.; Toyao, T.; Maeno, Z.; Ogura, M.; Nakazawa, N.; Inagaki, S.; Kubota, Y.; Shimizu, K. Formation and Reactions of NH₄NO₃ during Transient and Steady-State NH₃-SCR of NO_x over H-AFX Zeolites: Spectroscopic and Theoretical Studies. *ACS Catal.* **2020**, *10*, 2334–2344.
- (59) Ogura, M.; Sugiura, Y.; Hayashi, M.; Kikuchi, E. Reduction of Nitric Oxide with Methane on Pd/Co/H-ZSM-5 Catalysts: Cooperative Effects of Pd and Co. *Catal. Lett.* **1996**, *42*, 185–189.

- (60) Ruggeri, M. P.; Nova, I.; Tronconi, E.; Collier, J. E.; York, A. P. E. Structure-Activity Relationship of Different Cu-Zeolite Catalysts for NH_3 -SCR. *Top. Catal.* **2016**, *59*, 875–881.
- (61) Wang, P.; Jin, M.; Yu, D.; Bai, S.; Lei, L. Evolution Mechanism of N_2O for the Selective Catalytic Reduction of NO_x by NH_3 Over Cu-SSZ-13 Assisted Fe-BEA Catalysts. *Catal. Lett.* **2021**, *355*, 555–562.
- (62) Lee, J. H.; Jin, Y.; Ryu, T.; Soon, P.; Hwan, C.; Bong, S. Synthesis of Zeolite UZM-35 and Catalytic Properties of Copper-Exchanged UZM-35 for Ammonia Selective Catalytic Reduction. *Appl. Catal., B* **2017**, *200*, 428–438.
- (63) Wang, D.; Yao, Q.; Hui, S.; Niu, Y. Source of N and O in N_2O Formation during Selective Catalytic Reduction of NO with NH_3 over $\text{MnO}_x/\text{TiO}_2$. *Fuel* **2019**, *251*, 23–29.
- (64) González, J. M.; Villa, A. L. High Temperature SCR Over Cu-SSZ-13 and Cu-SSZ-13 and Fe-SSZ-13: Activity of Cu^{2+} and $[\text{CuOH}]^{1+}$ Sites and the Apparent Promoting Effect of Adding Fe into Cu-SSZ-13 Catalyst. *Catal. Lett.* **2021**, No. 52.
- (65) Fickel, D. W.; Lobo, R. F. Copper Coordination in Cu-SSZ-13 and Cu-SSZ-16 Investigated by Variable-Temperature XRD. *J. Phys. Chem. C* **2010**, *114*, 1633–1640.
- (66) Zones, S. I. Zeolite SSZ-13 and Its Method of Preparation. US Patent 4,544,538, 1985.
- (67) Deka, U.; Juhin, A.; Eilertsen, E.; Emerich, H.; Green, M. A.; Korhonen, S. T.; Weckhuysen, B. M.; Beale, A. M. Confirmation of Isolated Cu^{2+} Ions in SSZ-13 Zeolite as Active Sites in NH_3 -Selective Catalytic Reduction. *J. Phys. Chem. C* **2012**, *116*, 4809–4818.
- (68) Wang, D.; Jangjou, Y.; Liu, Y.; Sharma, M. K.; Luo, J.; Li, J.; Kamasamudram, K.; Epling, W. S. A Comparison of Hydrothermal Aging Effects on NH_3 -SCR of NO_x over Cu-SSZ-13 and Cu-SAPO-34 Catalysts. *Appl. Catal., B* **2015**, *165*, 438–445.
- (69) Džimbeg-Malčić, V.; Barbarić-Mikočević, Ž.; Itrić, K. Kubelka-Munk Theory in Describing Optical Properties of Paper (II). *Teh. Vjesn.* **2012**, *19*, 191–196.
- (70) Hickman, D. A.; Degenstein, J. C.; Ribeiro, F. H. Fundamental Principles of Laboratory Fixed Bed Reactor Design. *Curr. Opin. Chem. Eng.* **2016**, *13*, 1–9.
- (71) Cybulskis, V. J.; Smeltz, A. D.; Zvinevich, Y.; Gounder, R.; Delgass, W. N.; Ribeiro, F. H. Learning the Fundamentals of Kinetics and Reaction Engineering. *Chem. Eng. Educ.* **2016**, 202–210.
- (72) Fogler, H. S. *Essentials of Chemical Reaction Engineering*; Pearson Education, 2010.
- (73) Satterfield, C. N. *Mass Transfer in Heterogeneous Catalysis*; MIT Press: Cambridge, MA, 1970.
- (74) Harris, J. W.; Verma, A. A.; Arvay, J. W.; Shih, A. J.; Delgass, W. N.; Ribeiro, F. H. Consequences of Product Inhibition in the Quantification of Kinetic Parameters. *J. Catal.* **2020**, *389*, 468–475.
- (75) Brandenberger, S.; Kröcher, O.; Tissler, A.; Althoff, R. The State of Art in Selective Catalytic Reduction of NO_x by Ammonia Using Metal-Exchanged Zeolite Catalysts. *Catal. Rev.* **2008**, *50*, 492–531 DOI: 10.1080/01614940802480122.
- (76) Carl, P. J.; Larsen, S. C. EPR Study of Copper-Exchanged Zeolites: Effects of Correlated g- and A-Strain, Si/Al Ratio, and Parent Zeolite. *J. Phys. Chem. B* **2000**, *104*, 6568–6575.
- (77) Wang, D.; Gao, F.; Peden, C. H. F.; Li, J.; Kamasamudram, K.; Epling, W. S. Selective Catalytic Reduction of NO_x with NH_3 over a Cu-SSZ-13 Catalyst Prepared by a Solid-State Ion-Exchange Method. *ChemCatChem* **2014**, *6*, 1579–1583.
- (78) Liu, A.; Liu, L.; Cao, Y.; Wang, J.; Si, R.; Gao, F.; Dong, L. Controlling Dynamic Structural Transformation of Atomically Dispersed CuO_x Species and Influence on Their Catalytic Performances. *ACS Catal.* **2019**, *9*, 9840–9851.
- (79) Dědeček, J.; Wichterlová, B. Role of Hydrated Cu Ion Complexes and Aluminum Distribution in the Framework on the Cu Ion Siting in ZSM-5. *J. Phys. Chem. B* **1997**, *101*, 10233–10240.
- (80) Gao, F.; Washton, N. M.; Wang, Y.; Kollár, M.; Szanyi, J.; Peden, C. H. F. Effects of Si/Al Ratio on Cu/SSZ-13 NH_3 -SCR Catalysts: Implications for the Active Cu Species and the Roles of Brønsted Acidity. *J. Catal.* **2015**, *331*, 25–38.
- (81) Verma, A. A.; Bates, S. A.; Anggara, T.; Paolucci, C.; Parekh, A. A.; Kamasamudram, K.; Yezerets, A.; Miller, J. T.; Delgass, W. N.; Schneider, W. F.; Ribeiro, F. H. NO Oxidation: A Probe Reaction on Cu-SSZ-13. *J. Catal.* **2014**, *312*, 179–190.
- (82) Weitkamp, J.; Puppe, L. *Catalysis and Zeolites Fundamentals and Applications*; Springer-Verlag: Berlin, 1999.
- (83) Gao, F.; Walter, E. D.; Karp, E. M.; Luo, J.; Tonkyn, R. G.; Kwak, J. H.; Szanyi, J.; Peden, C. H. F. Structure-Activity Relationships in NH_3 -SCR over Cu-SSZ-13 as Probed by Reaction Kinetics and EPR Studies. *J. Catal.* **2013**, *300*, 20–29.
- (84) Ryu, T.; Kim, H.; Hong, S. B. Nature of Active Sites in Cu-LTA NH_3 -SCR Catalysts: A Comparative Study with Cu-SSZ-13. *Appl. Catal., B* **2019**, *245*, 513–521.
- (85) Wang, J.; Fan, D.; Yu, T.; Wang, J.; Hao, T.; Hu, X.; Shen, M.; Li, W. Improvement of Low-Temperature Hydrothermal Stability of Cu/SAPO-34 Catalysts by Cu^{2+} Species. *J. Catal.* **2015**, *322*, 84–90.
- (86) Baes, C. F.; Mesmer, R. E. *The Hydrolysis of Cations*; Wiley: New York, 1976.
- (87) Schreier, M.; Teren, S.; Belcher, L.; Regalbutto, J. R.; Miller, J. T. The Nature of “overexchanged” Copper and Platinum on Zeolites. *Nanotechnology* **2005**, *16*, S582–S591.
- (88) Albrecht, T. W.; Addai-Mensah, J.; Fornasiero, D. *Effect of pH, Concentration and Temperature on Copper and Zinc Hydroxide Formation/Precipitation in Solution*; Chemeca 2011: Engineering a Better World, 2011.
- (89) Hidmi, L.; Edwards, M. Role of Temperature and pH in $\text{Cu}(\text{OH})_2$ Solubility. *Environ. Sci. Technol.* **1999**, *33*, 2607.
- (90) Giordanino, F.; Vennestrøm, P. N. R.; Lundegaard, L. F.; Stappen, F. N.; Mossin, S.; Beato, P.; Bordiga, S.; Lamberti, C. Characterization of Cu-Exchanged SSZ-13: A Comparative FTIR, UV-Vis, and EPR Study with Cu-ZSM-5 and Cu- β with Similar Si/Al and Cu/Al Ratios. *Dalton Trans.* **2013**, *42*, 12741–12761.
- (91) Lu, C.; Qi, L.; Yang, J.; Zhang, D.; Wu, N.; Ma, J. Simple Template-Free Solution Route for the Controlled Synthesis of $\text{Cu}(\text{OH})_2$ and CuO Nanostructures. *J. Phys. Chem. B* **2004**, *108*, 17825–17831.
- (92) Singh, D. P.; Ojha, A. K.; Srivastava, O. N. Synthesis of Different $\text{Cu}(\text{OH})_2$ and CuO (Nanowires, Rectangles, Seed-, Belt-, and Sheetlike) Nanostructures by Simple Wet Chemical Route. *J. Phys. Chem. C* **2009**, *113*, 3409–3418.
- (93) Swanson, H. E. *Standard X-Ray Diffraction Powder Patterns*; National Bureau of Standards Monograph 25. U.S. Department of Commerce, 1972.
- (94) Scherrer, P. Estimation of the Size and Internal Structure of Colloidal Particles by Means of Röntgen. *Nachr. Ges. Wiss. Göttingen* **1918**, *2*, 96–100.
- (95) Patterson, A. L. The Scherrer Formula for X-Ray Particle Size Determination. *Phys. Rev.* **1939**, *56*, 978–982.
- (96) Lardinois, T. M.; Bates, J. S.; Lippie, H. H.; Russell, C. K.; Miller, J. T.; Meyer, H. M., III; Unocic, K. A.; Prikhodko, V.; Wei, X.; Lambert, C. K.; Getsoian, A. B.; Gounder, R. Structural Interconversion between Agglomerated Palladium Domains and Mononuclear Pd(II) Cations in Chabazite Zeolites. *Chem. Mater.* **2021**, *33*, 1698–1713.
- (97) Chen, P.; Moos, R.; Simon, U. Metal Loading Affects the Proton Transport Properties and the Reaction Monitoring Performance of Fe-ZSM-5 and Cu-ZSM-5 in NH_3 -SCR. *J. Phys. Chem. C* **2016**, *120*, 25361–25370.
- (98) Rizzotto, V.; Chen, P.; Simon, U. Mobility of NH_3 -Solvated Cu^{II} Ions in Cu-SSZ-13 and Cu-ZSM-5 NH_3 -SCR Catalysts: A Comparative Impedance Spectroscopy Study. *Catalysts* **2018**, *8*, No. 162.
- (99) Loiland, J. A.; Lobo, R. F. Low Temperature Catalytic NO Oxidation over Microporous Materials. *J. Catal.* **2014**, *311*, 412–423.